The thermal state of permafrost ~~in~~ under climate change on the Qinghai-Tibet Plateau ~~from~~ (1980 ~~to~~ -2022): A case study of the West Kunlun

Jianting Zhao[1,4], Lin Zhao[1,2,3*], Ze Sun[1,5], Guojie Hu[3], Defu Zou[3], Minxuan Xiao[1], Guangyue Liu[3], Qiangqiang Pang[3], Erji Du[3], Zhibin Li[1], Xiaodong Wu[3], Yao Xiao[3], Lingxiao Wang[1], Wenxin Zhang[4,6]

[1]School of Geographical Sciences, Nanjing University of Information Science &Technology, Nanjing 210044, China

[2]College of Resources and Environment, University of Chinese Academy of Sciences, Beijing 101408, China

[3]Cryosphere Research Station on the Qinghai–Tibetan Plateau, State Key Laboratory of Cryospheric Sciences, Northwest Institute of Eco-Environment and Resources, Chinese Academy of Sciences, Lanzhou 730000, China

[4]Department of Physical Geography and Ecosystem Science, Lund University, Lund 22362, Sweden

[5]School of Geography and Planning, Nanning Normal University, Nanning 530001, China

[6]School of Geographical and Earth Sciences, University of Glasgow, Glasgow, G12 8QQ, UK

Abstract: The thermal regime is a key indicator of permafrost evolution and thaw trajectories in response to climate change, ~~yet it~~ but remains ~~inadequately~~ poorly represented in global models. In this study, we applied the Moving-Grid Permafrost Model (MVPM)-an efficient and integrated numerical model~~, the Moving-Grid Permafrost Model (MVPM) was used~~ to simulate the permafrost thermal regime in West Kunlun (WKL), ~~which is approximately~~ a 55,669 km^2 region on the remote northwest Qinghai-Tibet Plateau characterized by ~~with~~ extreme arid climate conditions. To improve ~~enhance~~ computational efficiency. w~~W~~e employed clustering ~~approaches~~ methods and parallel computing techniques ~~to enhance computational efficiency.~~ The model was forced~~ing~~ ~~data,~~with remote-sensing-based land surface temperature (LST) ~~dating back to~~ data from 1980 onward (1 km spatial, monthly temporal resolution), reconstructed using machine learning techniques that ~~with a spatial resolution of 1 km×1 km and a temporal resolution of 1month, was constructed using machine learning techniques~~ that integrate field observations, satellite data and reanalysis products. MVPM maintained stability throughout the simulation, achieving high accuracy (±0.25 °C for ground temperature and ±0.25 m for active layer thickness), surpassing previously reported results.~~Our simulations achieved high accuracies of ±0.25°C for ground temperature and ±0.25 m for active layer thickness, significantly outperforming previous simulations reported to date.~~ From 1980 to 2022, LST increased by ~~The results indicated that the WKL experienced a pronounced~~

---

* Corresponding author: Lin Zhao (lzhao@nuist.edu.cn)

~~warming trend in LST, with~~ an average increase of 0.40°C per decade from 1980 to 2022. The responses of the permafrost regime to climate warming were closely related to the original thermal conditions shaped by historical climatic evolution. These responses exhibited a distinct altitude-dependent spatial variation and differed according to soil stratigraphic types. Despite ongoing thermal changes, ~~the thermal warming trend,~~ the spatial areal extent of permafrost remained relatively stable ~~across the WKL region~~ over the past 43 years, reflecting the delayed ~~slow and lagged~~ response of deep permafrost to ~~climate~~surface warming. These findings offer valuable insights into permafrost thaw trajectories and can improve projections of future permafrost degradation in data-scarce, high-altitude region. ~~are essential for enhancing our understanding of permafrost thaw trajectories, and improving projections of potential future consequences of permafrost degradation with greater accuracy.~~

1 Introduction

Permafrost covers about 40% of the Qinghai-Tibet Plateau (QTP), making it the largest high-elevation permafrost region in mid- to high-latitude areas, with an average altitude above 4000 m a.s.l (Zou et al., 2017). Observations of the ground thermal state provide clear evidence that permafrost warming has already led to thaw subsidence and widespread near-surface permafrost degradation in many areas on the QTP (Zhao et al., 2020, 2024; Biskaborn et al., 2019; Wang et al., 2022; Smi~~im~~th et al., 2022). These changes ~~potentially~~ may trigger climatic feedbacks on both local to global scales, with significantly consequences for ~~impacting~~ ecosystem, infrastructure, and communities on QTP (Schuur et al., 2015; Walvoord et al., 2016; Lafrenière et al., 2019; Cheng et al., 2019; O'neill, et al., 2020; Jin et al., 2021; Miner et al., 2021; Hjort et al., 2022). ~~Consequently~~Therefore, accurately ~~evaluating~~ assessing and understanding ~~characteristics of~~ current permafrost dynamics in response to climate variability is critical evaluating~~essential and highly valuable for assessing~~, predicting, and mitigating the impacts of climate change (Smith et al., 2022; IPCC, 2019, 2021).

Over the past few decades, ~~multiple~~ numerous field investigations have been ~~conducted~~carried out, and a monitoring network has been established on the QTP to monitor changes in permafrost thermal conditions (Zhao et al.,2010a, 2010b, 2017, 2019a, 2021). Many of these sites include borehole sensor arrays that ~~, which provide~~ measure~~ments~~ of ground profile temperature at~~as~~ depths of ~~deep as~~ 50 m or more ~~below the surface~~ (Zhao et al., 2019b, 2021). However, these observations are spatial limited ~~to discrete points~~, with most observation sites concentrated in easily accessible areas, such as along the Qinghai-Tibet Highway (QTH) and Qinghai-Tibet Railway (~~QTH~~QTR), leaving vast, remote region of ~~permafrost regions across the~~ QTP largely unmonitored~~, particularly in remote areas, largely unmonitored~~. To address this ~~research~~ gap, detailed process-based models have been widely developed to simulate hydrothermal processes in frozen soils. Despite these efforts, ~~However,~~ most of these models still struggle to accurately represent the thermal state of permafrost, leading to substantial errors in projections ~~predicting~~ of permafrost changes (Zhao et al., 2024). These inaccuracies are largely due to ~~This is attributed to~~ the simplified representations of ~~treatment of~~ soil properties and thermal processes in deep permafrost, driven by limited subsurface data and ~~a lack of detailed ground information and~~ insufficient long-term in situ ground temperature monitoring in deep permafrost (Sun et al., 2019; Zhao et al., 2020, 2024). Moreover, most models ~~these models primarily~~ focus on near-surface hydrothermal processes, typically constrained to the active layer within the upper 2–3 m. This limitation is particularly evident in large regional modeling at high spatial resolution, where ~~the~~ computational costs make it challenging to ~~demands of~~ apply~~ing~~ numerical models over broader spatial scales and deeper layers~~greater depths are considerable~~ (Smith et al., 2022). As a results, ~~Such~~ shallow simulations may inadequately ~~fail to accurately~~ capture changes in the thermal state of areas with thicker, colder permafrost, whereas deeper simulations ~~simulations extending to greater depths~~ more effectively represent the long-term thermal response to climate warming~~of permafrost to warming~~ (Sun et al., 2019; Zhao et al., 2020). In addition, uncertainties in the model forcing datasets further ~~also~~ contribute to biases in~~ the simulation~~ simulating ~~results of~~ hydrothermal processes in frozen ground (Yi et al., 2018; Guo et al., 2017; Hu et al., 2023). Previous studies have demonstrated that soil temperature projections from Earth system models (ESMs) outputs of the Coupled Model Intercomparison Project Phase 5 and 6 (CMIP5, CMIP6) tend to overestimate future permafrost changes (Koven et al., 2013; Lawrence et al., 2012; Slater and Lawrence, 2013; Burke et al., 2020). When air temperature and precipitation inputs to L~~l~~and surface models (LSMs) are improved, the estimated permafrost degradation rates decrease by approximately 29% (Lawrence et al., 2012). This highlights the necessity for high-resolution and more accurate model forcing datasets.

~~To address model deficiencies, we developed a new numerical permafrost model known as the Moving-Grid Permafrost Model (MVPM; Sun et al., 2019; 2022) in consideration of variations in thermal properties between frozen and thawed soil, unfrozen water content in frozen soil, ground ice distribution, thaw settlement of ground surface, and geothermal heat flow—factors often overlooked in existing models (Sun et al., 2022; Zhao et al., 2024). It was used to simulate the heat transfer processes effectively by capturing both the attenuation and time lag of heat transfer in deep permafrost at several borehole sites and limited regions along the QTH (Sun et al., 2019, 2022, 2023; Zhao et al., 2022), and showed sufficient accuracy to resolve the annual dynamics of ALT and~~

~~refreezing, as well as the evolution of ground temperatures in deeper layers, compared with long-term continuous soil temperature monitoring at various depths and ALTs.~~

To address deficiencies in existing models, the Moving-Grid Permafrost Model (MVPM; Sun et al., 2019, 2022) was developed to enhance the simulation of subsurface thermal dynamics in permafrost regions. Unlike conventional LSMs that use shallow or fixed soil layers, MVPM adopts a flexible vertical discretization scheme that better captures deep soil stratification and variability in ground ice content. It improves the simulation of freeze–thaw processes by applying the apparent heat capacity method, which more realistically represents gradual phase transitions, in line with field observations on the QTP. MVPM also explicitly incorporates geothermal heat flux as the lower boundary condition—an important factor often neglected in many LSMs, thereby improving the accuracy of long-term ground temperature simulations. In addition, the model includes a thaw settlement module, which is rarely represented in other permafrost models. This module simulates surface subsidence and landscape change driven by the melting of excess ground ice, processes that are critical to the evolution of permafrost terrain and the development of thermokarst features. These landscape changes have the potential to mobilize large quantities of previously frozen organic carbon from cold, ice-rich lowlands, thus intensifying the global permafrost carbon–climate feedback (Turetsky et al., 2015; Westermann et al., 2016; Jan et al., 2020). Together, these advancements allow MVPM to more effectively simulate both the attenuation and time lag of thermal signals in deep permafrost, making it well-suited for assessing permafrost thermal regimes under a changing climate. In our previous work, MVPM was successfully applied to simulate heat transfer processes at multiple borehole sites and regions along the QTH. The model demonstrated strong performance in reproducing both the seasonal dynamics of active layer thawing and refreezing, as well as long-term ground temperature evolution, when compared with multi-depth soil temperature records and active layer thickness (ALT) measurements (Sun et al., 2019, 2022, 2023; Zhao et al., 2022).

The accuracy of permafrost simulation results is ~~simulation results are more~~ closely tied related to the spatial resolution and quality ~~accuracy~~ of input dataset. Several studies have employed ~~utilized the~~ gridded datasets derived from in situ meteorological observations~~ measurements at meteorological stations~~, climate outputs from G~~g~~eneral C~~c~~irculation M~~m~~odels (GCMs), or ~~Earth System Models (~~ESMs~~)~~ as well as ~~or~~ reanalysis and assimilated datasets ~~as inputs~~ to simulate soil thermal regime dynamics over large spatial scales in the Circum-Arctic permafrost region (Jafarov et al., 2012; Westermann et al., 2013; Zhang et al., 2014; Fiddes et al., 2015). However, substantial ~~large~~ uncertainties remain in these climate forcing datasets, especially over the QTP,~~–~~ due to the harsh climate, complex terrain, and limited observations coverage ~~on the permafrost of QTP~~, these limitations makes ~~making~~ it difficult to reliably ~~challenging to~~ use such datasets to ~~these datasets to accurately~~ drive the MVPM for accurate simulation of permafrost thermal regimes on the QTP ~~simulating permafrost regimes on the QTP~~ (Hu et al., 2019; Qing et al., 2020; Yang et al., 2020). In addition, ~~Moreover,~~ gridded outputs from ESMs are typically provided at a spatial resolution of half-degree latitude/longitude or ~~coarser, which~~coarser which are insufficient to ~~cannot adequately~~ capture the high spatial variability of the ground thermal conditions in the heterogeneous ~~regime in~~ permafrost ~~areas~~ of the QTP (Zhang et al., 2013; Hu et al., 2023). In contrast, satellite remote sensing offer a powerful tool for region detection and monitoring of land surface characteristics that influence permafrost thermal dynamics ~~enables regional detection and monitoring of land surface conditions related to permafrost thermal properties~~ (Langer et al., 2013). High-resolution, satellite-driven numerical modeling provides a promising approach to assess permafrost thermal state with improved spatial and temporal fidelity. ~~Regionally refined, satellite-driven numerical models provide a promising approach for assessing permafrost thermal state dynamics with higher spatial and temporal resolution~~ (Westermann et al., 2015, 2017; Yi et al., 2018). This satellite-based approach has been successfully applied in various permafrost regions, ~~concept for permafrost thermal state modeling and assessment has been successfully applied in various permafrost regions worldwide,~~ including Alaska (Yi et al., 2018), Siberia (Langer et al., 2013; Westermann et al., 2017), and Canada (Zhang et al., 2013), demonstrating its potential for regional-scale, high-resolution permafrost monitoring. ~~. All these model results demonstrate that numerical modeling using remote-sensing data holds great potential for high-resolution permafrost monitoring on a regional scale. In the~~On the QTP permafrost region, Zou et al. (2017) and Cao et al. (2023) used MODIS Land Surface Temperature (LST) product as inputs data to an equilibrium model to map permafrost distribution. ~~mapped permafrost spatial distribution using the Moderate Resolution Imaging Spectroradiometer (MODIS) Land Surface Temperature (LST) product as input data for an equilibrium model.~~ Similarly, in our previous ~~simulations~~work, Zhao et al. (2022) evaluated and validated ~~demonstrated~~ the performance of the MVPM at a 1km spatial resolution using time-series MODIS LST data for a localized region (less than 280 km^2). ~~modeling scheme at a spatial resolution of 1 km, driven by a time series of MODIS LST data for a localized region (less than 280 km^2) on the QTP.~~

In this study, we aim to enhance and expand the MVPM to enable ~~facilitate~~ accurate, large-scale mapping of the ground thermal regime and ~~its~~ their spatiotemporal changes under recent climate warming.~~in response to recent climate changes.~~ We develop an integrated framework ~~that~~ combining~~es~~ numerical modeling, field observations, remote~~ly~~ sensing~~ed~~ data, and reanalysis data to simulate permafrost dynamics ~~, allowing simulation of permafrost thermal distribution~~ at a 1 km

×1 km spatial resolution. Soil properties were parameterized using a geomorphology map and filed measurements. ~~We used a geomorphological map and field measurements to parameterize soil properties.~~To address the computational challenges of large-scale thermal modeling, we employed a clustering approach that groups climate forcing and soil thermal types, and used ~~properties into discrete types, and we implement~~ parallel computing to simulate ~~enable the efficient simulation of~~ tens of thousands of grid cells efficiently. ~~within a reasonable time frame.~~ The MVPM modelling scheme was applied ~~was then run~~ over a 43-year period (1980–2022) across WKL ~~(Fig. 1)~~ in the northwest QTP, where ~~field measurements of~~ ground temperature and ALT observations are available for ~~validating simulation results~~validation. Finally, we ~~aimed to~~ quantitatively analyzed ~~the~~ spatiotemporal patterns of the thermal regime across diverse environmental settings.~~dynamics of the thermal regime across different environmental settings under climate change from 1980 to 2022 based on the modeling output.~~

2 Study area

The WKL permafrost survey area (78.8–81.4°E, 34.5–36.0°N) ~~,~~ is located ~~situated~~ in the northwestern of the QTP, with an elevation range of 4200-6200 m above sea level a.s.l (see Fig. 1a). ~~and spans~~It covers an area of ~~–~~approximately 4.37×10^3 km^2 (Zhao et al., 2019b). This region experiences ~~has~~ a cold and arid continental climate, as the Pamir-Tian Shan-Kunlun Mountain system ~~s~~ acts as an orographic barrier, restricting ~~limiting~~ moisture influx from both the westerlies and monsoons (Cannon et al., 2016; Baldwin and Vecchi, 2016). Meteorological observations from Tianshuihai (TSH) ~~the~~ automatic weather station (AWS) (TSH, 81.4°E, 36.0°N, at 5019 m a.s.l) at ~~Tianshuihai (TSH, 81.4°E, 36.0°N, at 5019 m a.s.l) for the period~~ from 2015to-2018 show ~~report~~ a mean annual temperature of ~-6°C and mean annual precipitation of ~103.5mm (Zhao et al., 2021). Over 78%~~(~81mm)~~ of this precipitation (~81mm) falls during May-September, and the summer temperature stays above zero degrees 0°C, averaging around 5.8°C ~~(~5.8°C)~~ (Zhao et al., 2021). The glacial and periglacial landforms, such as ~~(e.g.,~~ block fields, stripes, and stone rings~~)~~ are well developed throughout the region (Wu et al., 2018). Vegetation is sparse, ~~Typically, the vegetation is~~ dominated by sparse alpine desert, while much of the land surface is barren due to persistent wind erosion ~~and the most of exposed landforms are barren due to wind erosion~~ (Li et al., 2012; Wang et al., 2016; Zhao et al., 2019). The topsoil is generally ~~was~~ dry and loose, composed mainly ~~primarily composed~~ of Quaternary aeolian erosion deposits ~~resulting from aeolian erosion~~ (57.68%, see detail in table 1), ~~which~~ consisting of coarse-grained ~~sediments~~material such as gravel and sand (see Figure 1b). Permafrost ~~in WKL~~ is well-developed in WKL, comprising ~~encompassing~~ both discontinuous and continuous types, and covers ~~the areal extent occupying~~ approximately 93% of the total area (Li et al., 2012; Zhao et al., 2019). Continuous ground temperature monitoring ~~monitoring of a borehole~~ at the TSH comprehensive observatory (ZK015, 59 m in depth, 79.54°E, 35.36°N, see Fig. 1b) has revealed notable permafrost warming. Between 2010 and 2017, temperature at the depth of 15m increased at a rate of 0.11°C per decade ~~indicates strong changes in the thermal state of permafrost, with a warming rate of 0.11°C per decade between 2010 and 2017 at a depth of 15 m~~ (Zhao et al., 2021, Hu et al., 2023).

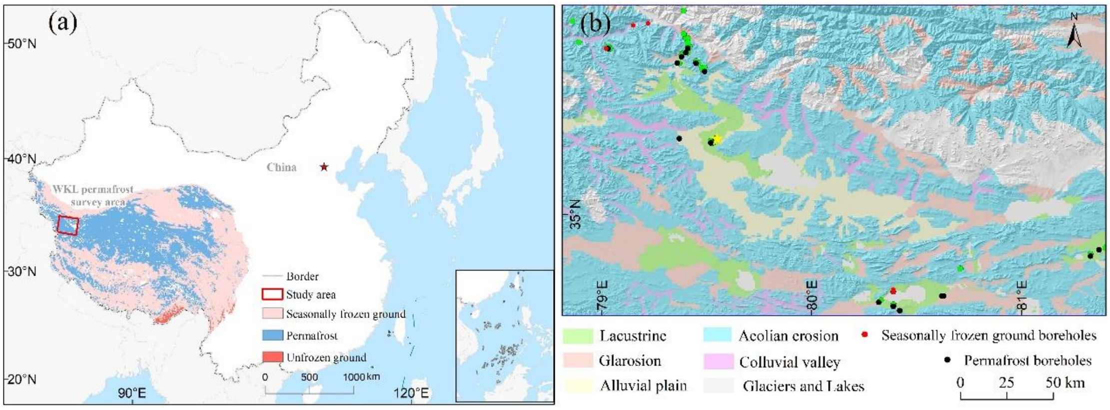

Figure 1. (a) ~~The g~~Geographical location of the West Kunlun (WKL) permafrost survey area, ~~is~~ overlaid on the frozen ground type distribution map from Zou et al. (2017) and the background maps based on Wen et al. (2024). (b) The WKL ~~permafrost~~ survey area mainly includes five stratigraphic classes distinguished in the ground thermal modelling (Sect. 3.2.2), along with ~~and~~ boreholes sites containing ~~with~~ in situ observations (Sect. 3.3) ~~, which are~~ used for model calibration and validation. The yellow star marks the location of an ~~indicates~~ automatic weather stations (AWS); red dots represent ~~denote~~ monitoring boreholes in seasonally frozen ground; black dots indicate monitoring boreholes located in permafrost; and green dots represent thaw depth measurements derived from ~~obtained using~~ ground-penetrating radar (GPR) surveys~~technology~~.

3 Methodology and data

3.1 The Moving-Grid Permafrost Model

~~The Moving-Grid Permafrost Model (MVPM) is used to simulate the permafrost thermal regime and its dynamics under climate change. This is a transient, one-dimensional, nonlinear heat transfer model that accounts for phase changes in soil pore water, variations in thermal properties between frozen and thawed soil, geothermal flux, and the effects of ground ice. The model also includes a settlement module, which was not part of our previous model configuration (Zhao et al.,~~

~~2022). Soil temperature dynamics are simulated by numerically solving the one-dimensional nonlinear conductive heat equation using the finite difference method (Schiesser, 1991; Westermann et al., 2013; Sun et al., 2019). The MVPM has recently been used to simulate permafrost thermal dynamics at several borehole sites across the QTP (Sun et al., 2019, 2022, 2023; Zhao et al., 2022). Detailed descriptions of the model and its parameterization are provided in these companion studies.~~

The Move-Grid Permafrost Model (MVPM) is a numerical framework that combines a moving-grid (Lagrangian) scheme with the heat conduction equation to dynamically track freeze–thaw fronts and adjust the vertical grid accordingly. This approach reduces numerical diffusion and more accurately captures latent heat effects and delayed thermal responses in deep permafrost layers (Sun et al., 2019, 2022). MVPM integrates key processes—including unfrozen water content, variable thermal properties, geothermal heat flux, and excess ice—within an efficient moving-grid framework, enabling improved simulation of deep soil heat transfer not typically represented in most land surface models.

MVPM includes both a heat conduction module and a settlement module, which are coupled to simulate time series of ground temperature with the land surface as the upper boundary. Its heat conduction physics is comparable to that of widely used models such as GIPL2.0 (Dmitry et al., 2017) and CryoGrid2.0 (Westermann et al., 2013). The change in ground temperature and internal energy is governed by Fourier's law of heat conduction, accounting for latent heat release or absorption due to phase change within an observed freezing range of −0.3 to 0 °C. Water and vapor movement are not included; thus, soil water content changes only through freezing and thawing. Soil temperature dynamics are solved numerically using the one-dimensional nonlinear heat conduction equation and the finite difference method (Schiesser, 1991; Westermann et al., 2013; Sun et al., 2019).

3.2 Model operation

3.2.1 Model forcing

~~Similar to our previous study (Zhao et al., 2022), a time series of remotely sensed LST was used to drive the MVPM. Specifically, an 8-day mean LST dataset covering the entire QTP, with a spatial resolution of 1 km × 1 km (hereafter referred to as "LST_Zou"), was used for the period from 2003 to 2019, provided by Zou et al. (2014, 2017). This dataset was created by integrating in situ observations with satellite-based LST from the Moderate Resolution Imaging~~

~~Spectroradiometer (MODIS). In this work, to fully account for the impact of historical climate on the thermal regime evolution of the WKL permafrost region, three statistical algorithms were employed to extend the LST_Zou dataset back to 1980: the least squares linear regression (LR) model (Xing et al., 2023), the random forest regression (RFR) model (Breiman et al., 2001), and the multiple linear regression (MLR) model (Jiao et al., 2023). The LR model assumes a linear relationship between air temperature (AT) and LST over long-term periods. For the RFR and MLR models, we considered eight auxiliary explanatory variables that influence LST: air temperature (AT), precipitation (Pre), skin temperature (ST), soil temperature in the topsoil layer (0–10 cm) (ST_1), fractional cloud cover (CFC), surface radiation budget (SRB), leaf area index (LAI), and digital elevation model (DEM). Details on these variables, including their resolution and relevant references, are provided in Table 1. The main steps for reconstructing monthly LST from 1980 to 2022 are as follows:~~

Similar to our previous study (Zhao et al., 2022), a time series of remotely sensed LST was used to drive the MVPM. Specifically, we used a modified MODIS LST product developed by Zou et al. (2014, 2017), which partially accounts for surface influences such as snow cover, vegetation, and cloud presence through a cloud-gap filling algorithm and calibration with AWS observations from representative permafrost regions in the central QTP. Validation at three typical permafrost sites with different surface types (alpine steppe, alpine meadow, and alpine desert) showed strong agreement between the modeled and observed LST, with R^2 values ranging from 0.91 to 0.93 and RMSE values around 3°C. Further evaluation at the TSH AWS site in the WKL region during the observation period from 2016 to 2018 confirmed the product's reliability, with an R^2 greater than 0.90 and an RMSE of 2.09 °C, demonstrating its effectiveness in capturing spatial variations in LST across the QTP.

In this study, we further refined the Zou et al. (2017) product to reconstruct historical LST data prior to 2003, extending the dataset back to 1980 using machine learning approaches. Three statistical models were employed: least squares linear regression (LR; Xing et al., 2023), random forest regression (RFR; Breiman et al., 2001), and multiple linear regression (MLR; Jiao et al., 2023). The LR model assumes a long-term linear relationship between air temperature (AT) and LST. For the RFR and MLR models, eight auxiliary variables known to influence LST were incorporated: AT, precipitation (Pre), skin temperature (ST), soil temperature in the top 0–10 cm (ST_1), fractional cloud cover (CFC), surface net radiation budget (SRB), leaf area index (LAI), and digital elevation model (DEM). Detailed descriptions of these variables, including their spatial resolution and data sources, are provided in Table 1. The main steps for reconstructing monthly LST from 1980 to 2022 are as follows:

(1) Pre-processing

All input variables were ~~first~~ resampled to a spatial resolution of 1 km × 1 km using the nearest neighbor method ~~resolution~~ to match that of LST_Zou ~~using the nearest neighbor method~~. ~~Monthly averages were then calculated from daily data, and missing values were filled by interpolating nearby data.~~ Monthly averages were then calculated from the available data (which varied in temporal resolution across datasets), and missing values were filled by interpolating from nearby data. Notably, the latest downscaled air temperature (AT) and precipitation (Pre) data ~~AT and Pre data~~ provided by Qin et al. (2022) are only available up to 2019. To fill the data gap for 2020-2022, ~~Therefore, we performed~~ statistical downscaling was applied to AT and Pre ~~(Su et al., 2016) of AT and Pre~~ from the CN05.1 datasets, following the method described by -Su et al. (2016). ~~for the years 2020–2022.~~ CN05.1 is a gridded dataset developed ~~provided~~ by the China Meteorological Administration (CMA), offering daily ~~which includes key~~ meteorological variables ~~with~~ at a spatial resolution of 0.25°. For more details, refer to Wu et al. (2017). ~~and a daily temporal resolution. For further details, refer to the comprehensive description by Wu et al. (2017).~~ Additionally, since the earliest available remote sensing-based leaf area index (LAI) data ~~LAI data~~ begins in 1982, values for 1980-1981 were filled by assuming no change and using the average LAI from 1982-1986.~~we assumed no changes for the initial two years and averaged data from 1982 to 1986 to fill in the gaps.~~

(2) Model training and test

Data from 2003 to 2019 were used for model training. ~~were selected as the training sample for the models. I~~n the LR model, AT was used as the input variable, with ~~and~~ LST_Zou ~~served~~ as the target output ~~variable~~. For the MLR and RFR models, eight auxiliary variables (see Table 1) were used as inputs, with LST_Zou as the output variable. The dataset was randomly divided into ten subsets: 10% of the samples were reserved for validation, and the remaining 90% were used for training. ~~one subset, comprising 10% of the samples, was retained for validation, while the remaining nine subsets (90% of the samples) were used for model training~~. This process was repeated 2,000 times to ensure robustness. Model performance was evaluated using four metrics: ~~The model's accuracy was assessed using four metrics: the coefficient of determination (~~R^2~~)~~, ~~root mean square error (~~RMSE~~)~~, ~~mean absolute error (~~MAE~~)~~, and bias (Zhao et al., 2022). See Fig. 3 for details.

(3) Dataset generation

The monthly values of the eight auxiliary variables from 1980 to 2022 (see Table 1)~~(see Table 1) from 1980 to 2022~~ were used as input to the trained LR, MLR, and RFR model from step (2). This enabled the generation of a continuous monthly LST time series starting from 1980.~~variables for the three models (LR, MLR, and RFR) established in step (2), enabling the generation of a time series of monthly LST starting from 1980.~~

Table 1: Summary of the data sources used for the linear regression model (LR), random forest regression model (MLR), and multiple linear regression model (RFR) to generate monthly land surface temperature from 1980 to 2022.

Variable name	Data span	Resolution and Horizontal coverage	Data resource and availability	Reference
LST_Zou	2003-2019	8-day (QTP)	--	Zou et al. (2017)
AT Pre	1961-2019	Daily/1km×1km (China)	https://doi.org/10.1594/ PANGAEA.941329	Qin et al. (2022)
ST	1950-present	Hourly/~9km×9km (global)	ERA5-Land Reanalyst https://cds.climate.copernicus.eu/datasets/reanalysis-era5-land?tab=overview/cdsapp#!/dataset/reanalysis-era5-land?tab=overview	Muñoz-Sabater et al. (2021)
ST_1	1979-present	6 hour /0.312°×0.312°/ 0.204°×0.204° (global)	NCEP Climate Forecast System Reanalysis (CFSR) https://rda.ucar.edu/datasets/ds093.0/dataaccess/	Saha et al. (2010)
CFC SRB	1979-present	Monthly/ 0.25°×0.25° (global)	EUMETSAT, CM SAF https://wui.cmsaf.eu/safira/action/viewDoiDetails?acronym=CLARA_AVHRR_V003	Karlsson et al. (2023)
LAI	1982-2022	8-day/0.05° from AVHRR, 500 m from MODIS (global)	Global Land Surface Satellite (GLASS) and MODIS http://www.glass.umd.edu/ https://modis.gsfc.nasa.gov/data/datapr	Liang et al. (2020)

			od/mod15.php	
DEM	--	90m (global)	SRTM/https://cgiarcsi.community/data/srtm-90m-digital-elevation-database-v4-1	Jarvis et al. (2008)
Glacier	--	--	National Snow and Ice Data Center https://nsidc.org/data/nsidc0770/versions/6	Guo et al. (2015)
Lakes	--	--	National Tibetan Plateau Data Center https://data.tpdc.ac.cn/	Zhang et al. (2019)

Note: LST_Zou is an enhanced land surface temperature (LST) product for the QTP permafrost zone, derived from in situ observations and MODIS satellite data. AT refers to air temperature; Pre to precipitation; ST to skin temperature; ST_1 to soil temperature at the top layer (0–10 cm); CFC to fractional cloud cover; SRB to surface radiation budget; LAI to leaf area index; and DEM to Shuttle Radar Topography Mission (SRTM) digital elevation model data.

3.2.2 Ground thermal properties

~~The stratigraphy plays a crucial role in determining variations in lithology, mineralogy, water retention, and ice content in permafrost regions (Wang et al., 2018; Sheng et al., 2019). These factors significantly influence ground thermal dynamics, controlling both soil temperature and the permafrost thermal regime (Westermann et al., 2017). In this study, soil thermal properties were parameterized using a vector geology map from the digital geomorphological database of western China, at a scale of 1:1,000,000 (Zhou and Cheng, 2007), along with ground temperature and thaw depth measurements. We identified five predominant stratigraphies within the WKL permafrost survey area, for which we defined "typical" subsurface stratigraphies based on available ground temperature observations and thaw depth measurements (Sect. 3.3). A list of major Quaternary deposits is provided in Table 2, and their spatial distribution (Fig. 1b) is based on Zhou et al. (2007), gridded to 1 km × 1 km to match our simulation resolution.~~

~~The ground thermal properties of different stratigraphic classes are estimated using observations from a representative borehole. Four of the five stratigraphic classes are represented by two or more in situ measurement sites (see details in Table 2). However, no ground temperature or ALT measurements are available for the alluvial plain. Therefore, we use properties from the lacustrine plain class as a reference. Thermophysical properties (e.g., lithological composition, ground ice content, organic matter content, dry bulk density) of distinct soil profile layers were~~

~~measured or assessed through field surveys, laboratory measurements, and on-site analyses of soil samples obtained from 28 borehole cores (depths ranging from 7.5 to 59 m). Detailed information about the boreholes and soil samples can be found in Li et al. (2012), Li et al. (2014, 2015), and Zhao et al. (2019). Additionally, a 1 km × 1 km resolution ground ice distribution map (down to a depth of 10 m) by Zou et al. (2024), and data on the vertical distribution of ice content for various sedimentary classes on the QTP based on representative borehole cores from field investigations and geological surveys (Zhao et al., 2010), were used to estimate water content for each stratigraphic class.~~

~~Depth-specific soil profile thermophysical parameters (thermal conductivity and heat capacity) for each stratigraphic class were estimated by calibrating the modeled permafrost temperature and thaw depth against observed data. Calibration of ground thermal properties was performed using a numerical solution to an inverse problem, which aimed to minimize the discrepancy between simulated and observed ground temperatures by adjusting thermal properties (Marchenko et al., 2024; Nicolsky et al., 2016). This calibration method is described in detail in Nicolsky et al. (2007, 2016), with an example of soil thermal properties optimization procedures provided in Zhao et al. (2022) and Marchenko et al. (2024).~~

In our modeling framework, we incorporated detailed thermophysical characterization of the subsurface based on measurements from 15 boreholes across the West Kunlun (WKL) permafrost survey area, with depths ranging from 15 to 59 m. Core samples, field observations, and borehole logs (Li et al., 2012; Zhao et al., 2019) indicate that ground ice content in the WKL region varies between 5% and 50%, depending on the type of Quaternary sediment. Higher ice contents are typically found in fine-grained glarosional and lacustrine sediments due to enhanced segregation ice formation, while coarse-grained alluvial and colluvial deposits generally show lower ice content. Vertically, ice-rich layers are consistently observed near the upper boundary of permafrost, typically between 2 and 3 m depth. Ice content tends to increase slightly between 3 and 10 m and remains relatively stable below 10 m (Zhao et al., 2010).

Depth-specific thermophysical parameters (thermal conductivity and heat capacity) for each stratigraphic class were estimated by calibrating modeled permafrost temperature and thaw depth against borehole observations. Calibration was performed using a numerical inverse modeling approach that minimizes the difference between simulated and observed ground temperatures by adjusting the thermal properties (Marchenko et al., 2024; Nicolsky et al., 2016). This method is detailed in Nicolsky et al. (2007, 2016), with examples of soil thermal property optimization provided in Zhao et al. (2022) and Marchenko et al. (2024).

Site-level stratigraphic and thermophysical data were spatially upscaled using vector-based geomorphological classification maps of western China at a 1:1,000,000 scale (Zhou and Cheng, 2007). Five common stratigraphic classes in the WKL region—glarosional, alluvial plain, aeolian, colluvial valley, and lacustrine deposits—were identified. A summary of major Quaternary deposits is provided in Table 2, and their spatial distribution (Fig. 1b) is based on Zhou et al. (2007), gridded at 1 km × 1 km resolution to match our simulation scale.

Table 2: ~~List of~~ M~~m~~ajor geological classes and their association ~~with~~ borehole measurement sites. The second column indicates~~shows~~ the percentage of the study area covered by ~~represented by~~ each type of Quaternary sediment, while the third column lists the corresponding ~~'typical'~~ representative boreholes.

Quaternary sediments type	Percent %	Boreholes
Aeolian	57.68	ZK01, ZK02, ZK04, ZK12, ZK13, ZK16, K514+950, K520+050,
Glarosion	12.58	ZK06, ZK07
Alluvial plain	5.96	ZK08
Lacustrine plain	5.05	ZK14, ZK15, ZK17, ZK18, ZK30, ZK31
Colluvial valley	3.67	ZK09, ZK04
Modern Glaciers	12.54	Excluded from the model
Lakes	2.52	Excluded from the model

3.2.3 Model computational domain, boundary condition and initialization

The model~~'s~~ resolution is governed by that ~~determined by the resolution of~~ the input dataset. Specifically, the computational ~~simulation~~ domain has a spatial resolution of 1 km × 1 km and temporal resolution of monthly, encompassing ~~covering~~ the entire WKL permafrost survey area, which ~~contains~~ spans approximately 55,669 km^2. Consistent with ~~Similar to the setup used in~~ our previous simulations (Zhao et al., 2022), the vertical domain ~~computation~~ for each spatial grid cell extends to a depth of 100 m, ~~and is~~ discretized into 282 layers. ~~Specifically,~~ T~~t~~he ~~layer~~ thickness of these varies ~~ranges~~ from 0.05 m in the upper 4 m to 0.5 m for in the deeper layers. ~~the remaining soil layers down to 100 m.~~

~~-~~For each modelling grid cell, the ground thermal regime is~~ was~~ simulated using site-specific ground stratigraphy and a time series of LST as upper boundary condition. ~~forcing time series of LST.~~ At the lower boundary (100 m depth)~~a depth of 100 m within the soil column~~, the Neumann ~~lower boundary~~ condition ~~was applied~~is applied to represent ~~specify~~ the geothermal heat flux, set at a constant value of ~~.~~0.0724 W/m². this value is derived from measurements obtained ~~A constant geothermal heat flow of 0.0724 W/m² was assumed, based on measurements~~ from a 700 m deep borehole near the WKL permafrost survey area (see details in Hu et al., 2000).To estimate a realistic initial temperature profile, a model spin-up is conducted using climate forcing from the early simulation years.~~ performed to achieve steady-state conditions based on the forcing in the initial model years~~. Steady state conditions are considered achieved when the temperature differences at all soil layers between consecutive annual cycles is less than 0.0001°C. This equilibrium profile is then adopted as the initial condition for subsequent transient modelling. ~~The criterion for reaching a steady-state soil temperature profile is an equilibrium temperature difference of less than 0.0001° C at all soil levels between successive annual cycles. This steady-state profile is then used as the initial condition for subsequent modelling.~~

3.2.4 Model implementation

After e~~E~~xcluding lake and glacier grids, simulations were conducted for ~~approximately~~ 47,284 grid cells. To improve computational efficiency, a spatial cluster analysis approach was adopted following Cable et al (2016). Grouping grid cells based on simulated in climate forcing and soil thermal properties. Instead of simulating each grid cell individually, cluster ere used as repetitive units.~~ were used for computation in the study area. To reduce model running time, we employed a spatial cluster analysis approach (Cable et al., 2016) to group cells based on climate forcing and soil thermal properties. This method allowed us to simulate these clusters rather than processing each pixel individually.~~

To characterize the upper boundary LST forcing, a harmonic function was used to fit the time series (see Sun et al., 2019 for details). The fitted coefficients (initial annual mean temperature, change rate, annual amplitude, and initial phase angle) were used to group climate forcing into distinct clusters. These were ~~Specifically, we mimic the variation in upper boundary condition LST series using a harmonic function (see Sun et al., 2019 for details). Based on the fitted coefficients (initial annual mean temperature, change rate, annual amplitude, and initial phase angle), we categorized the climate forcing of grid cells into several distinct clusters.~~ c~~C~~ombined with five soil thermal property classes (see Table 1), resulting ~~this resulted~~ in 13,248 unique input-data combinations for the WKL ~~permafrost survey area~~region. This approach reduce the number of simulations of just ~~These combinations account for only~~ 28.02% of the total model grid cells, ~~remarkable~~ remarkably reducing computation time. Similar cluster-based methods has been successfully ~~spatial cluster approaches have been~~ applied in Canada (Zhang et al., 2013, 2014), Alaska (Cable et al., 2016), and the Swiss Alps (Fiddes et al., 2015).

3.2.5 Simulation results diagnose

To assess long-term ~~For analysing~~ changes in the thermal state of permafrost over the past 43 years, ~~we use~~ K~~k~~ey diagnostics were extracted from the modelled vertical ground temperature profile down to 50 m. These include ~~depth to represent the thermal state of permafrost and the active layerALT. Specifically, we focus on~~ the mean annual ground temperature at a depth of 15 m (MAGT 15m), which corresponds to the depth of zero annual amplitude (ZAA) on the QTP (Jin et al., 2008; Zhao et al., 2010b), as well as the temperature at the top of permafrost (TTOP). Additional depths were also evaluated against available borehole observations. ~~We also consider other depths where we compare our simulations with borehole observations.~~

The active layer thickness (ALT) was estimated ~~To assess changes in ALT, we calculated ALT using~~ linear interpolation to identify ~~determine~~ the maximum depth of the 0°C isotherm over the thawing period of the year (Liu et al., 2020). Following Zhao et al. (2022) and Wu et al. (2018), model ~~grid~~ cells were classified as permafrost if the maximum temperature of any soil layer at a grid point was ⩽ 0°C for two consecutive years. Seasonally frozen ground was identified from the remaining cells where the minimum soil temperature of any layer during the same period was ⩽ 0°C. Cells that did not meet either criterion were classified as unfrozen ground.

3.3 Field~~iled~~ investigation and borehole monitoring datasets

Extensive scientific research and long-term monitoring programs have been conducted in WKL region over the past two decades. A comprehensive monitoring system has been established WKL by the Cryosphere Research Station, Chinese Academy of Sciences (CRS-CAS) (Zhao et al., 2015, 2019b, 2021). These detailed data sets significantly enhance our understanding of processes and support modeling efforts in the WKL (Li et al., 2012; Zhao et al., 2017, 2019, 2021). Below, we briefly describe the in-situ data sets from CRS-CAS used in this study.

3.3.1 The Tianshuihai (TSH) comprehensive observatory

The TSH comprehensive observatory is located in the central-northern part of the WKL permafrost survey area (see Fig. 1a). The Quaternary deposits in this region are primarily lacustrine, consisting of fine-grained sediment from an ancient lake that dried up in the Lower Pleistocene (Li et al., 1991). Since October 2015, an ~~automatic~~ AWS has been measuring key meteorological variables, including hourly air temperature at 2 m, 5 m, and 10 m, relative humidity, upward and downward shortwave and longwave radiation, wind speed, and precipitation. Additionally, ground temperature data have been automatically recorded since 2010 at depths of 3 m, 6 m, 10 m, and 20 m from a 59 m deep borehole (ZK015, 79.54°E, 35.36°N, see Fig. 1b) (Zhao et al., 2021). The LST at TSH is estimated using a continuous series of measurements (since October 2015) of downward and upward longwave radiation, applying the Stefan-Boltzmann law (see Hu et al., 2024 for details), providing~~. This provide~~s a robust basis for validating satellite datasets and ground thermal modeling (see Sect. 4.1.1).

3.3.2 Borehole in situ data sets

~~Outside~~Beyond the TSH ~~comprehensive~~ observatory, 27 boreholes have been ~~,~~ drilled across the WKL permafrost survey area to monitor the thermal regime. These boreholes range in depth ~~to depths ranging~~ from 7.5 to 33 m and are distributed across the various geomorphic units, soil types, and vegetation zones, covering ~~, have been installed across the WKL permafrost survey area to monitor the thermal regime (see Fig. 1b). These boreholes are distributed across various geomorphic, soil, and vegetation conditions, spanning~~ elevations from 4200 to 5200 m. Detailed information about these boreholes is provided in Zhao et al. (2019) and Li et al. (2012). 15 of these boreholes, is instruments with ~~Thermistor~~ thermistor sensors (accuracy of ± 0.1°C)~~, calibrated to an accuracy of 0.1°C, are strategically~~ placed ~~along the cables of these boreholes~~ at depths of 3 m, 6 m, 10 m, and 20 m (Zhao et al., 2021) and manual ground temperature measurements have been conducted ~~.~~ 1- to 2-year intervals since 2010 using a digital multimeter. ~~Additionally, ground temperatures have been manually measured using a digital multimeter at intervals of 1 or 2 years since 2010 in 15 boreholes with diverse ground surface conditions. For this study,~~ In this study, data from these ~~we used~~ 15 boreholes with ground temperature observations for model calibration and validation. The remaining boreholes were used to support the spatial modeling of permafrost distribution and serving as reference points for identifying permafrost ~~served as additional evidence for evaluating the~~ presence or absence ~~of permafrost in spatial permafrost distribution modeling.~~

3.3.3 Thaw depth measurement data sets

During fieldwork in September 2010, when seasonal thaw depth reach their annual ~~the~~ maximum ~~thaw depth was reached,~~ ground-penetrating radar (GPR) was used to manually measure thaw depth at 45 sites, ~~45 manual thaw depth measurements were conducted using GPR technology.~~ ~~Most~~ most of which were ~~these measurements were taken near drill~~ located near boreholes (see Fig. 1b). The methodology and results are comprehensively described in Zhao et al. (2019). ~~The thaw depth measurements from summer 2010 are thoroughly documented in Zhao et al. (2019).~~ After excluding measurements that overlapped within a 1 km grid, ~~we used~~ a ~~25~~total 25 unique thaw depth measurements were retained ~~distinct thaw depth measurements~~ for model validation.

3.4 Additional validation datasets

In addition to validating the site-based observations (Sec. 3.3), we ~~also~~ further evaluated model ~~our model's~~ performance in permafrost distribution by comparing it with four representative permafrost maps developed over ~~over the WKL permafrost survey region using four typical permafrost distribution maps from~~ different periods~~. These maps include~~: i) A 1980s permafrost map of the QTP at a 1:3,000,000 scale.~~ permafrost map of the QTP~~ compiled by the Lanzhou Institute of Glaciology and Geocryology, CAS (Li and Cheng, 1996); ii) A comprehensive 2000s map of glaciers, permafrost, and deserts in China at 1:4,000,000 scale, produced~~ a~~ ~~comprehensive 1:4,000,000 scale map of glaciers, permafrost, and deserts in China created~~ by the Cold and Arid Regions Environmental and Engineering Research Institute, CAS (Wang et al., 2006); iii) A~~a~~ 2010 permafrost distribution map of the QTP (Cao et al., 2023); iv). A 2016 permafrost distribution map of the Tibetan Plateau (Zou et al., 2017). Both of the latter two maps have the same spatial resolution of 1 km².

4 Result

4.1 Forcing dataset

4.1.1 Comparison to in situ data

We implemented and compared three algorithms described in ~~from~~ Section 3.2.1 to identify the optimal model for reconstructing monthly LST data from 1980 onward. ~~and t~~The validation results are shown in Figure 2. Most data point ~~The majority of the samples~~ in the scatter plots clustered near the 1:1 line, ~~demonstrating~~ indicating a strong positive correlation ($R^2 > 0.90$) and ~~,~~ ~~which indicates~~ good agreement between the LST_Zou and the estimated LST values. The LR model ~~yielded~~ produced MAE~~ and RMSE~~ ~~values~~ of 2.05℃ and RMSE of 2.61℃, respectively. The MRL model showed slight improvement, with lower error metrics (MAE = 1.16℃, RMSE = 1.55℃). However, the RFR model outperformed the others, producing the lowest errors (MAE = 0.87℃, RMSE = 1.26℃).

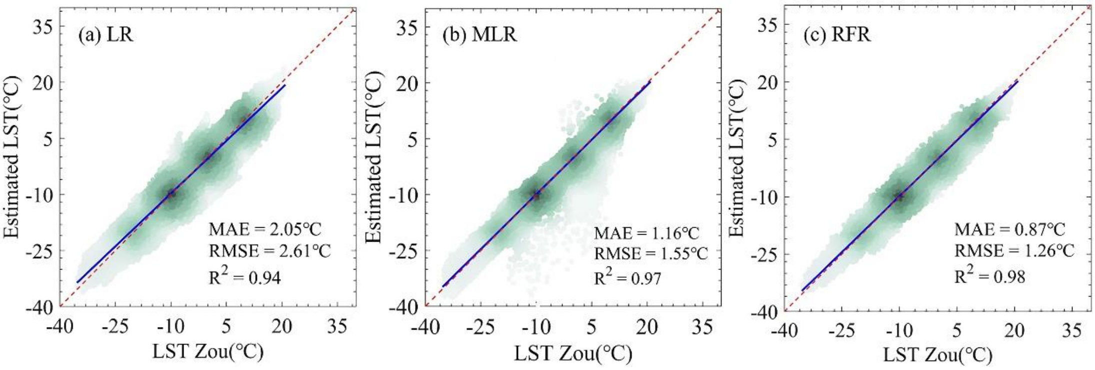

Figure 2: Scatterplots of estimated monthly LST using (a) LR: linear regression model, (b) MLR: multiple linear regression model, and (c) RFR: random forest regression model during the validation stage (10-fold cross-validation; see details in Sect. 3.2.1). The best linear fits are shown in blue, while the 1:1 line is represented in red. Error metrics are provided in the bottom right corner of each graph.

Figure 3 compares the mean annual cycle of LST estimated by the three statistical models (LR, MLR, and RFR) with LST_Zou and in situ monitoring data from the TSH AWS over the period ~~for the period~~ 2016–2018. All four datasets display a consistent mean annual cycle with the in situ data/ ~~observations, although~~ However, LST_Zou and Era5-land LST shows a systematic cold bias, particularly during July, August, and September. The ~~monthly~~ LST estimated from the three algorithms slightly reduce this cold bias, with the RFR model performing the best. Despite this improvement, ~~However,~~ a residual cold bias in LST_Zou remains noticeable in the same months. Overall, t~~he LST time series generated by~~ the RFR model-generated LST time series ~~-~~closely aligns with in situ measurements and demonstrates sufficient accuracy for subsequent ground thermal modeling. Therefore, the RFR-derived monthly time series ~~was~~ was adopted as ~~used~~ as input for the ground thermal modeling in the following simulation analsys~~sections~~.

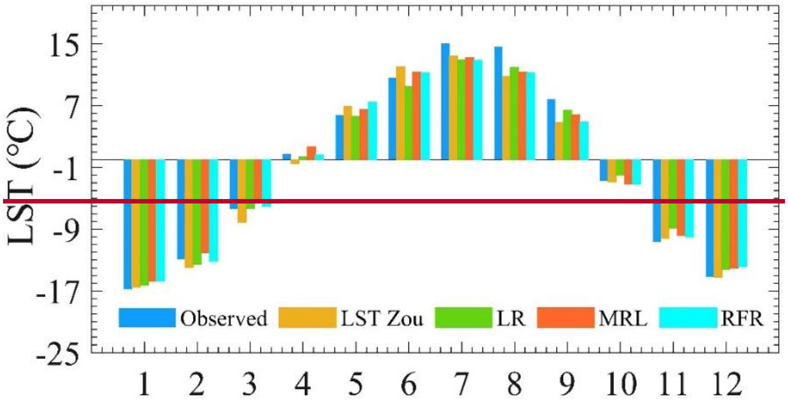

~~**Figure 3: Satellite-derived LST (LST_Zou), estimates from three different algorithms (LR,**~~

~~MLR, and RFR), and measured at the TSH AWS for the monthly average during periods when in situ measurements are available (see Sect. 3.3.1).~~

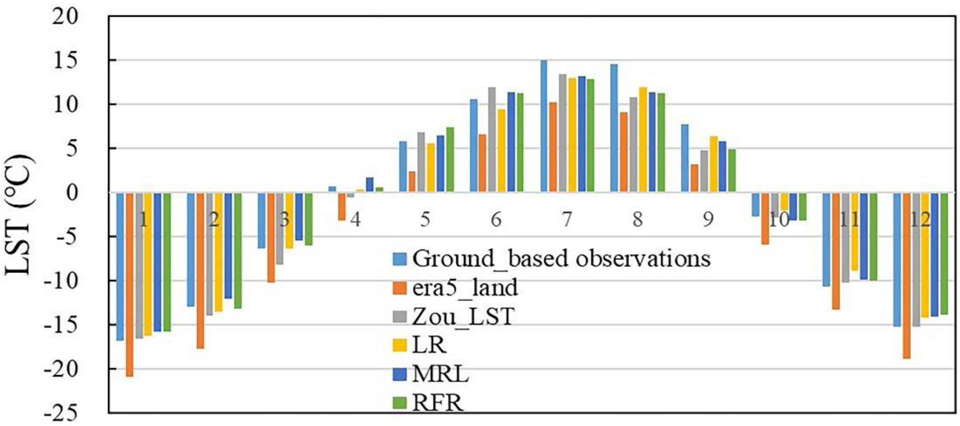

Figure 3: Monthly average LST values from satellite-derived data (LST_Zou), ERA5-Land, three algorithm estimates (LR, MLR, and RFR), and in situ measurements from the TSH AWS were compared for periods with available observations between 2016 and 2018 (see Sect. 3.3.1).

4.1.2 Spatiotemporal variability of forcing datasets

Figure 4 shows the regional average of annual LST anomalies relative to the 1980–2022 mean. The results reveal a consistent positive trend of +0.40°C per decade over the WKL region during this period. Interdecadal analysis highlights a remarkable warming trend in the mid-1980s, which then slowed slightly from the 2000s, during which LST deviations were relatively smaller. In the last decade, only positive anomalies were recorded, with 2016 exhibiting the largest positive deviation (+1.45°C) compared to the 1980–2022 climate average.

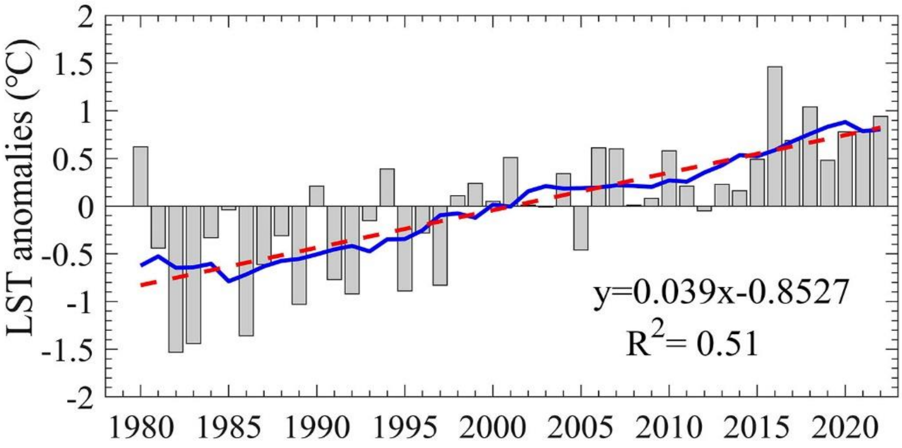

Figure 4: Time series of regional average annual LST anomalies in the WKL permafrost survey area from 1980 to 2022. The 9-year moving average is depicted with a blue line, while the linear trend, calculated using standard linear regression (with long-term changes based on the slope of the regression), is shown with a red dashed line. The anomalous LST series are obtained by subtracting the mean LST from 1980 to 2022.

To further assess regional ~~examine the regional distribution of~~ LST anomalies in WKL, Figure 5 shows decadal deviations from the 1980-2022. ~~presents the spatial patterns of anomalous LST for four decades (1980s, 1990s, 2000s, and 2010–2022) relative to the 1980–2022 average.~~ In the 1980s, most of region ~~the WKL~~ (63.25%) exhibited negative anomalies between -1.5°C and -0.5°C, with only 0.46% mainly at high-elevation mountainous areas falling below -1.5°C. The 1990s saw ~~while 36.3% had anomalies between -0.5°C and 0°C. A small fraction (0.46%), primarily in high-elevation mountainous areas, experienced the largest negative anomalies (-2.0°C to -1.5°C). From the 1980s to the 1990s,~~ a drastic warming ~~occurred across WKL~~, with 90.95% of the region shifting to near-normal levels (–0.5°C to 0°C). ~~showing anomalies between -0.5°C and 0°C in the 1990s.~~ By the 2000s, warming intensified: 83.78% of WKL showed positive anomalies (0°C to 0.5°C), and 4.34% exceeded 0.5°C. ~~11.87% of WKL experienced negative anomalies between -0.5°C and 0°C, while 83.78% saw positive anomalies between 0°C and 0.5°C. Notably, 4.34% of the region recorded the highest positive anomalies (0.5°C to 1.0°C).~~ Between 2011 to 2022, ~~From 2011 to 2022, a pronounced rise in LST was observed~~ warming became more prononanced, with 63.97% of the region above ~~experiencing anomalies greater than~~ 0.5°C, and some ~~areas, particularly in~~ high-~~elevatio~~ altitude zones surpassing ~~n mountainous regions, exceeding~~ 1.0°C.

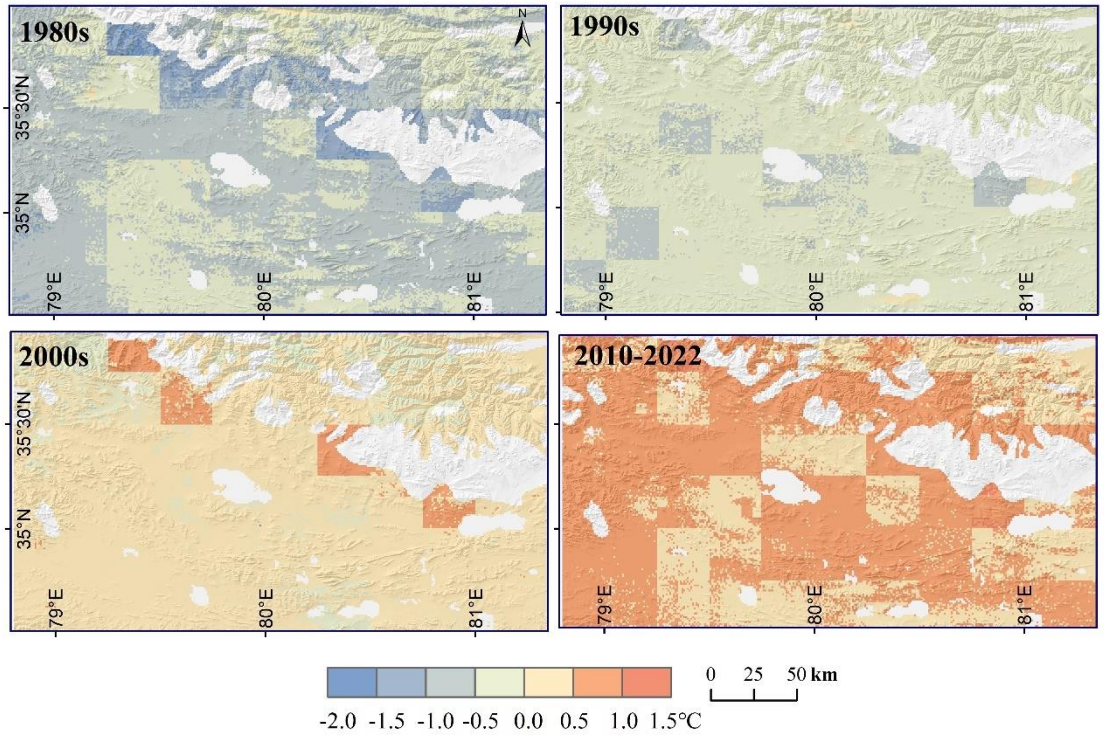

Figure 5: Maps of decadal anomalous LST patterns over the WKL permafrost survey area for the 1980s, 1990s, 2000s, and 2010–2022, relative to the 1980–2022 average. The anomalous LST patterns are calculated by subtracting the mean LST of 1980–2022. Glaciers and lakes are excluded and shown in white.

4.2 Modeled the thermal state of permafrost

4.2.1 Model validation

To validate ~~ensure that~~ the model's representation of ~~accurately represents~~ large-scale ground thermal conditions, the model outputs were compared with available in situ datasets (Fig. 1, Sect. 3.3) including ~~.~~MAGT ~~This comparison includes ground temperature measurements~~ at a depth of 10 m (MAGT10m) from 15 sites and ALT data from 11 sites in year 2010, and thaw depth measurements from 25 sites in the same time, as well as four permafrost distribution maps from various periods.

Ground temperatures: The comparison between observed and modeled MAGT10m at 15 permafrost boreholes shows that 93.3% (14 out of ~~/~~15) of the data points cluster around the best-fit line, with deviations within ±0.25°C (Fig. 6a). The analysis indicates a strong overall agreement between measured and modeled MAGT10m for temperatures above -1°C, with an error of 0.10°C or less. However, for MAGT10m below -2°C, the model exhibits a slight cold bias, particularly in areas with lacustrine sediments in the lowland regions of central WKL, where ground temperatures vary drastic due to complex local factors (Fig. 6b). Despite this, the deviations between observed and simulated temperatures within 0.3°C. Overall, the comparison suggests that the MVPM effectively replicates the measured MAGT10m, capturing the spatial variability of the validation area with an r of 0.98 ($p < 0.01$), and achieving an MAE of 0.12°C and 0.15°C.

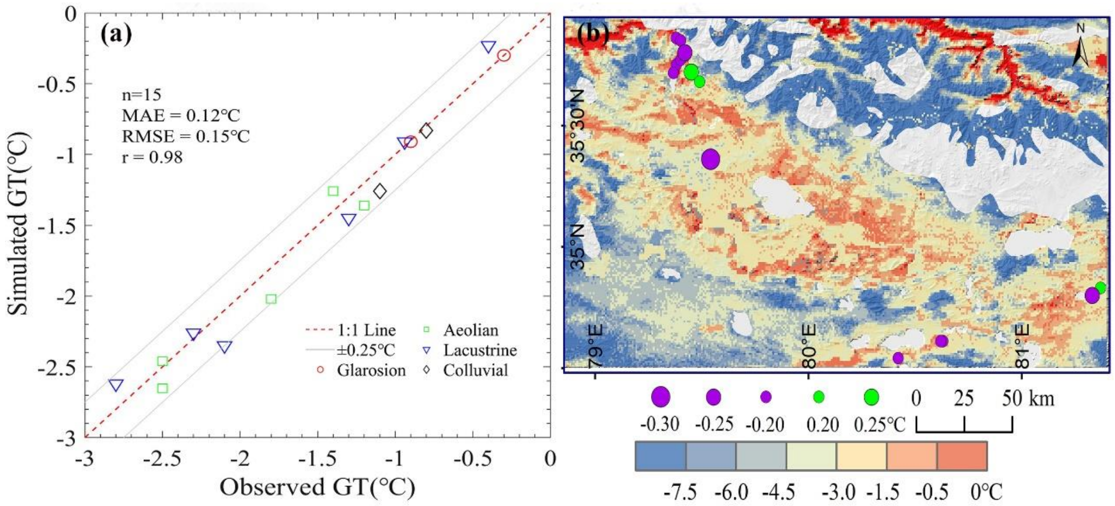

Figure 6: (a) Scatter plot comparing borehole-observed (Zhao et al., 2019b; Li et al., 2012) and modeled mean annual ground temperature at a depth of 10 m (MAGT10m) for~~ the year~~ 2010. Different symbols ~~represent~~ denote various soil stratigraphic classes (Glarosion, Aeolian, Lacustrine, Colluvial). Grey ~~shading~~ indicates biases within ±0.25°C, and the 1:1 line is shown in red. (b) Map showing spatial distribution of the modeled MAGT10m for 2010. Circle sizes and colors indicate the temperature differences between borehole-observed and modeled MAGT10m at the nearest 1 km grid point. Seasonally frozen ground is marked in red, and glaciers and lakes are depicted in grey.

Active layer thickness (thaw depths): The scatter plot and spatial map comparing measured and modeled ALT at 11 sites and thaw depths at 25 sites are shown in Figure 7. The comparison indicates that the model generally reproduces the range of ALT across WKL effectively. At ~~Simulated values for~~ 72.7% of the site (8 out of ~~/~~11), the simulated ALT values ~~of the sites align~~ closely match the observations, with ~~with the best fit, exhibiting~~ deviations of ±0.25 m ~~from~~ of the measurements (Fig.7a). Notably, for the Aeolian sediment class, characterized by relatively shallow ALT ~~which has small ALT values~~ around 2 m, ~~the agreement is excellent,~~ the model performs exceptional well, showing minimal bias (⩽0.05 m), which suggests that the model ~~with a relatively small bias of 0.05 m or less, indicating~~ that the modeling procedure is suitable for Aeolian sediments. However, the model underestimates ALT by 0.25 m in lacustrine sediments near lake areas, where measured ALT exceeds 3 m (Fig. 8c).

A similar pattern is ~~occurred~~ modelled in thaw depths, 91.3% of the modeled values (21 out of 23) fall within ±0.25 m of the observations (Fig. 7b). ~~where 91.3% (21/23) of the values cluster around the best fit, with deviations of ±0.25 m (Fig. 7b).~~ For thaw depths above 3 m, the model also shows underestimation, with the largest deviations reaching up to 0.5 m in northern marginal permafrost areas (Fig. 7c).

Overall, ~~although~~ despite slightly lager biases (>0.25 m) at a few locations, the results suggest that the model reliably reproduces the spatial variations in ALT and thaw depth across ~~there are relatively higher biases above 0.25 m at certain locations, the comparison~~ the results suggests that the ~~curren~~t model reliably reproduces the spatial variations in ALT and thaw depth across the the major geomorphological units of the WKL region. ~~can realistically reproduce the differences in ALT (thaw depth) between the main geomorphological units in the WKL region,~~ the model achieves~~ing~~ an r value of 0.96 (0.94) and an MAE of 0.13 m (0.16 m) for ALT and 0.16 m (0.18 m) for thaw depth.

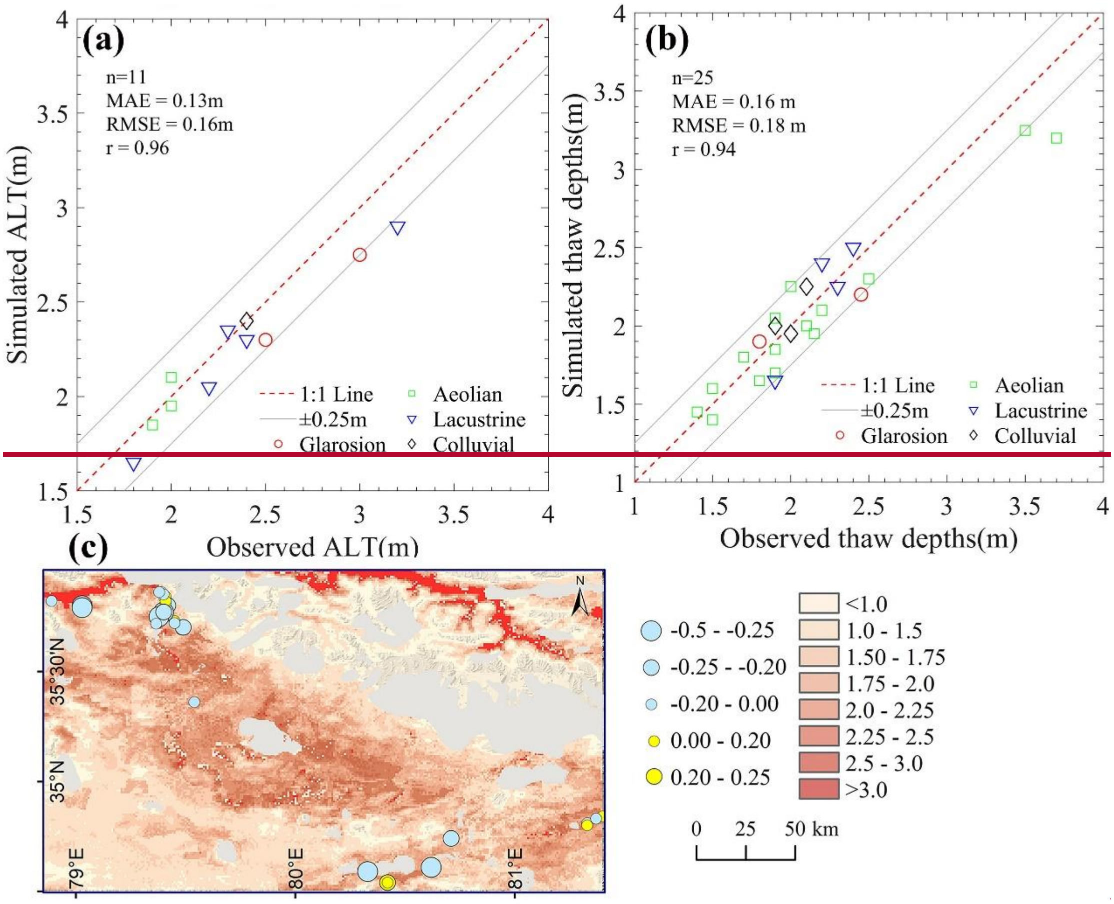

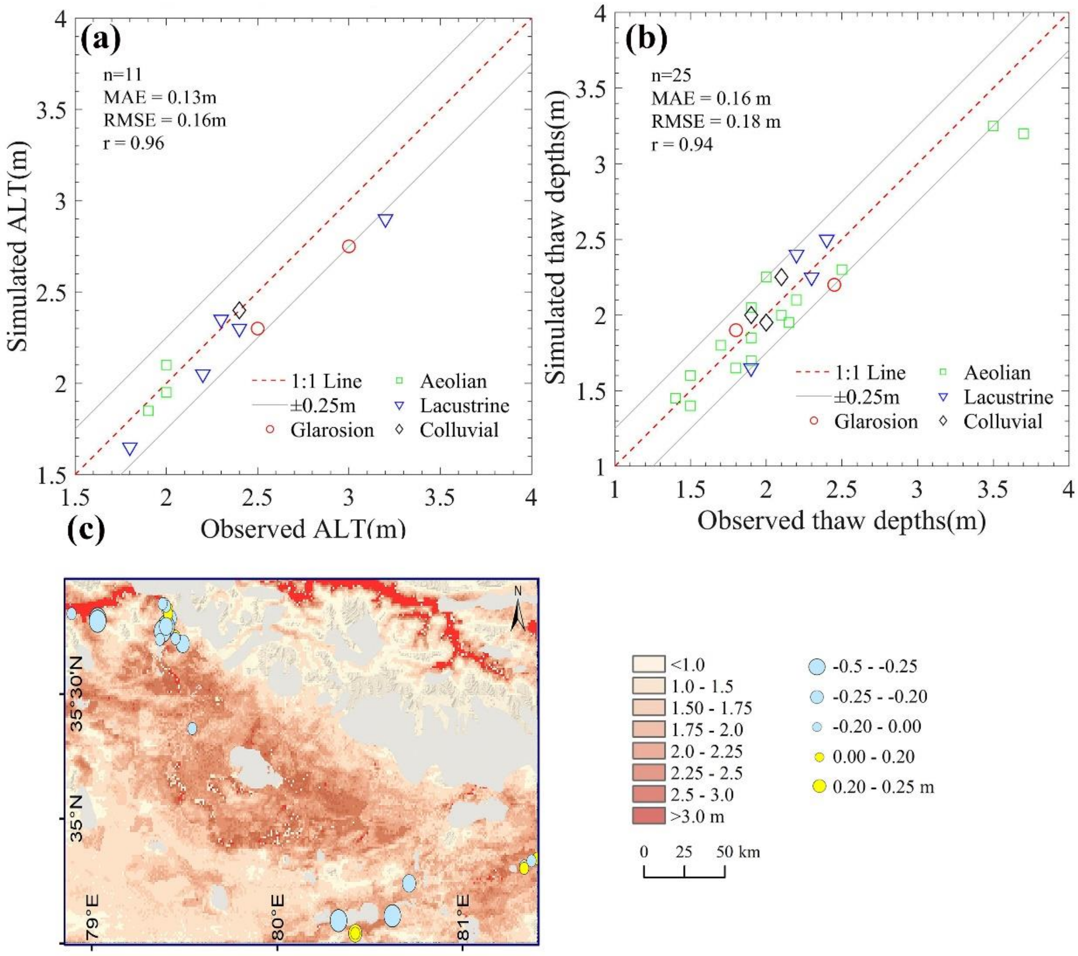

Figure 7: (a) Scatter plot comparing borehole- observed active layer thickness (ALT) in 2010 (Zhao et al., 2019b; Li et al., 2012) with modeled values. (b) Same as (a), but for thaw depths (Zhao et al., 2019). Biases within ±0.25 m are indicated in grey, and the 1:1 line is shown in red. (c) The modeled spatial distribution of ALT and thaw depths in 2010. The sizes and colors of the circles represent the deviation between borehole (GPR) observed ALT (thaw depths) and the corresponding model grid cell nearest to each observation site (within 1 km). Seasonally frozen ground is depicted in red, while glaciers and lakes are shown in grey.

Permafrost distribution: Figure 8 compares four typical frozen soil type maps of the ~~over~~ WKL with the corresponding outputs from our simulation ~~outputs~~. In this analysis, 28 boreholes (see details in Fig. 1 and Sect. 3.3) serve as evaluation points to verify the presence or absence of spatial permafrost distribution. The results indicate that while the maps by Li and Cheng (1996) and Wang et al. (2006) capture the general presence of permafrost ~~can identify permafrost distribution~~ across the WKL region, they fail to accurately delineate areas of seasonally frozen ground (Fig. 8a-c). ~~Additionally~~ Notably, these two maps show notably discrepancies in the distribution of frozen ground types in northeastern WKL, where permafrost is depicted, while our modeled outputs identify seasonally frozen ground (Fig. 8i-j).

In contrast, the maps by Cao et al. (2023) and Zou et al. (2017), along with our simulations, consistently display an accurate pattern of permafrost distribution, correctly identifying nearly all locations of permafrost and seasonally frozen ground, except for one site near lakes in southern WKL (Fig. 8c-d, g-h). However, small mismatches remain: compared to our simulations, Cao et al. (2023) and Zou et al. (2017) overestimate the extent of seasonally frozen ground by 1.84% and 1.61%, respectively, designating certain areas as seasonally frozen where our model indicates permafrost (Figs. 8k–l). ~~a slight discrepancy of 1.84% (1.61%) exists between the maps by Cao et al. (2023) and Zou et al. (2017) and our simulations regarding the areal extent of seasonally frozen ground. These maps delineate certain areas as seasonally frozen ground, while our simulations classify them as permafrost (Fig. 8k-l).~~ Additionally, ~~Furthermore,~~ our simulations indicate that 0.61% (Cao) and 0.58% (Zou) ~~0.61% (0.58%)~~ of the central lowland region as seasonally frozen ground, whereas both maps categorize these areas as permafrost (Figs. 8k–l).~~of the central lowland area of WKL contains scattered seasonally frozen ground, whereas the maps by Cao et al. (2023) and Zou et al. (2017) categorize these areas as permafrost (Fig. 8k-l)~~.

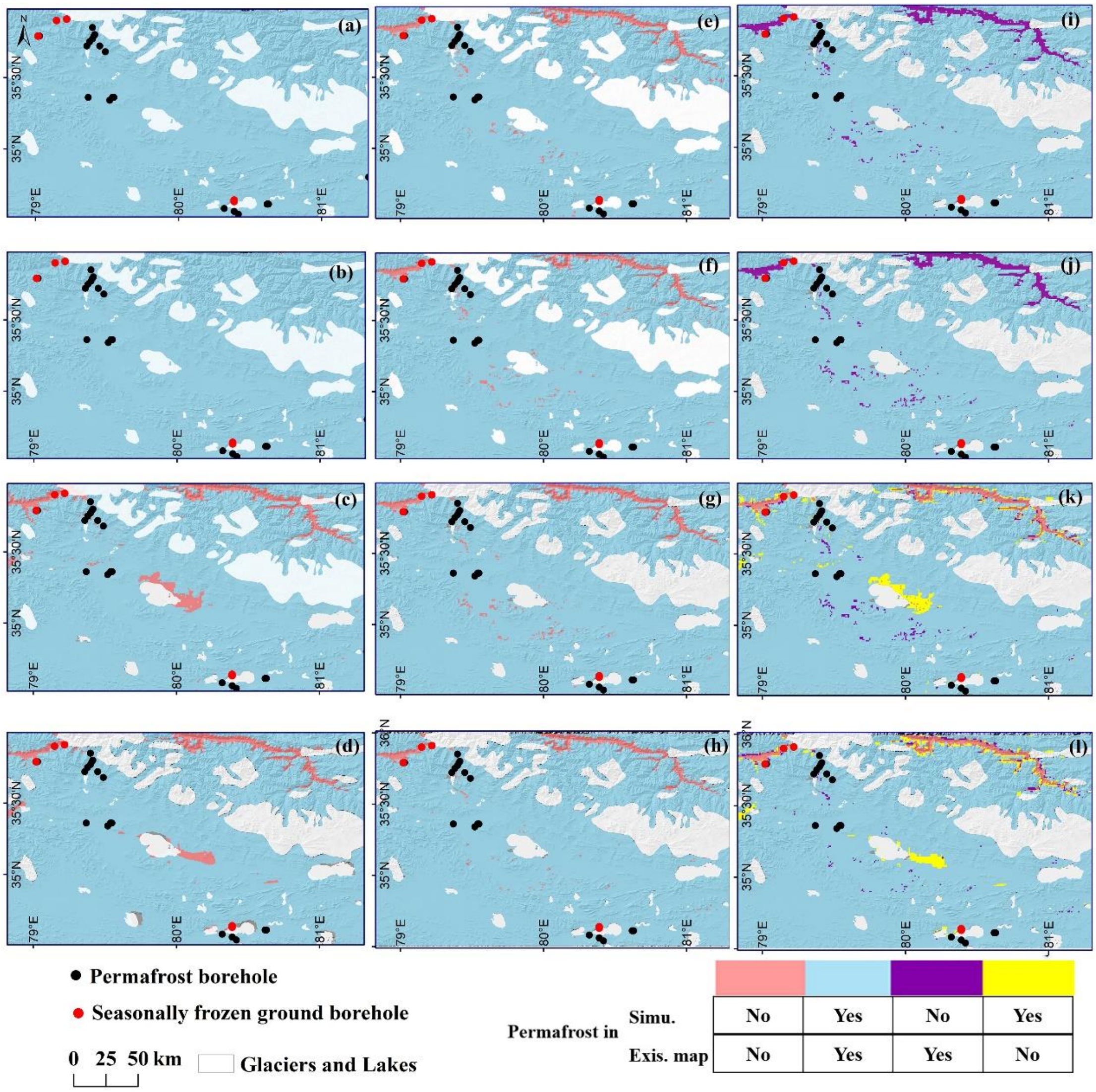

Figure 8: Spatial distribution of frozen ground type in the WKL permafrost survey area as depicted by four different maps from various periods: the 1980s (Li et al., 1996), (b) the 2000s (Wang et al., 2006), (c) 2010 (Cao et al., 2023), and (d) after 2010 (Zou et al., 2017) (left panels ~~(a) Li and Cheng (1996), (b) Wang et al. (2006), (c) Cao et al. (2023), and (d) Zou et al. (2017) (left panels)~~. The corresponding modeled outputs are presented in the middle panels (e-h), while the spatial inconsistencies between the existing maps and our model outputs for each period are illustrated in the right panels (i-l).

4.2.2 Initial thermal status of permafrost condition

To investigate how the thermal state of permafrost evolves with ongoing climate change, it is essential to first understand the characteristics of its initial conditions. Figure 9 presents the modeled initial status of MAGT15m, TTOP, and ALT for the year 1980. The results indicate drastic spatial variability in the ground thermal regime across the WKL permafrost survey area. The modeled MAGT15m decreases with elevation~~markedly with increasing elevation~~ with ~~.~~ t~~T~~he highest ~~average MAGT15m, approximately~~ around 0.5°C simulated in ~~, is found in~~ central low-elevation areas (below 4800 m a.s.l.), the coldest, ~~while the coldest average MAGT15m,~~ below -10°C, occurs in high-elevation regions (6000 m a.s.l.). ~~Additionally,~~ S~~s~~light variations ~~in the modeled MAGT15m are observed~~ across different soil stratigraphic classes (see Fig. 9c). The lowest average MAGT15m, around -3.5°C, is found in the Aeolian sedimentary class, while the relatively warmer average temperature of -1°C is modeled in the Alluvial plain sedimentary class.

A similar distribution pattern is evident for the modeled TTOP, although TTOP values generally ~~across the WKL permafrost survey region is~~ slightly lower than MAGT15m values (see Fig. 10d-f). Likewise, ~~the ground temperature distribution pattern,~~ the modeled ALT show a ~~across the WKL also shows a~~ strong dependence on elevation (Fig. 9j). In low-elevation areas (below 5400 m a.s.l.), modeled ALT ranges from 2.5 m to 3.0 m, with some localized regions exceeding 3.0 m. at higher elevations, ALT decreases progressively, dropping below 1.0 m, and approaches 0 m in areas ~~In contrast, ALT gradually decreases in high-elevation areas to less than 1.0 m, and it is modeled at 0 m in most regio~~ns above 6000 m a.s.l., where ground temperatures remain below freezing year-round. ALT also varies markedly across stratigraphic classes: the Alluvial sediments class exhibits the greatest average ALT, while the Glarosion class shows the shallowest (Fig. 9i). ~~Furthermore, remarkable variation in modeled ALT values is simulated across different ground stratigraphic classes, with the largest modeled average ALT occurring in the Alluvial sediments class and the lowest in the Glarosion sedimentary class (see Fig. 9i).~~

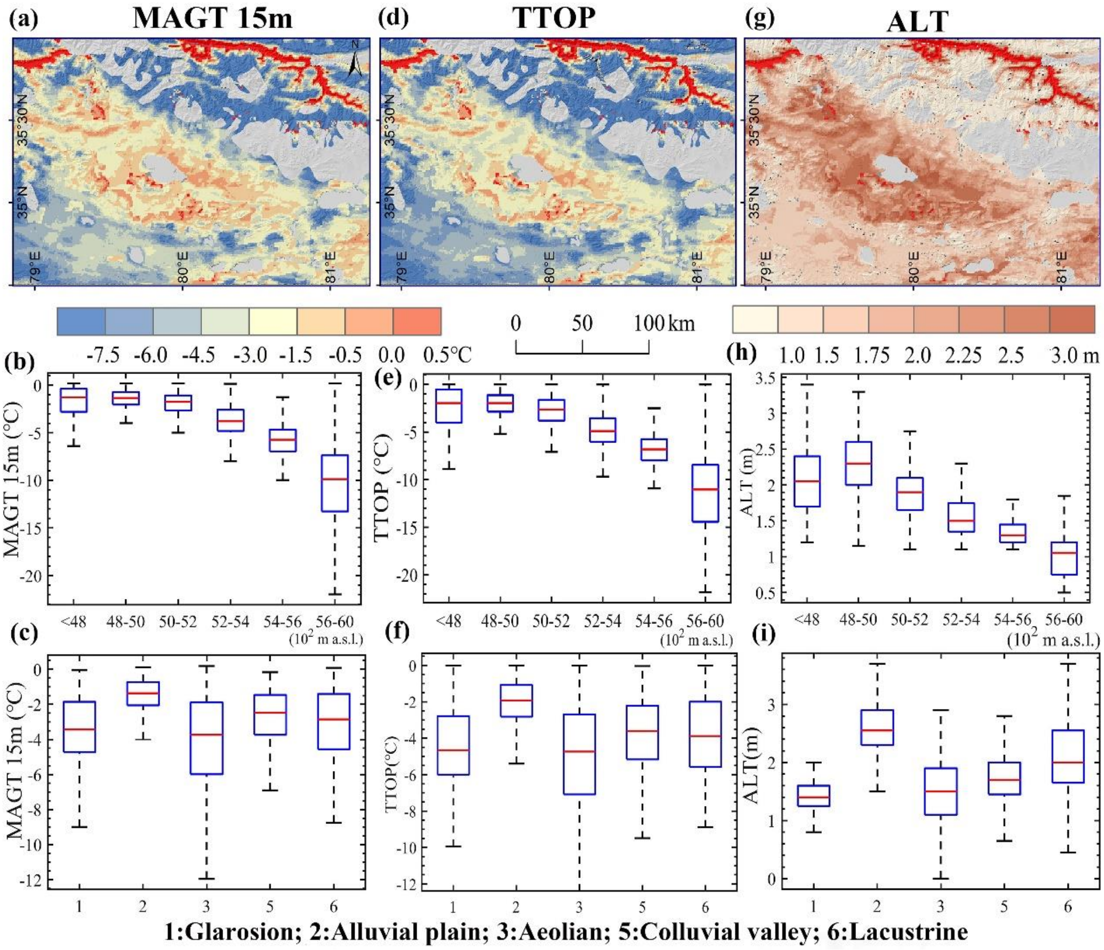

Figure 9: Spatial distribution of the simulated MAGT15m (first column, a-c), TTOP (second column, d-f), and ALT (third column, g-i) from the initial model simulation output for the year 1980. Seasonally frozen ground is depicted in red, while glaciers and lakes are shown in grey (first row). The middle row presents boxplot maps of MAGT15m, TTOP, and ALT, categorized by different elevations (ranging from 4300 m a.s.l. to 6000 m a.s.l., excluding certain areas). The third row categorizes the data by soil stratigraphic classes: Glarosion, Alluvial plain, Aeolian, Colluvial valley, and Lacustrine. In the boxplots, the top and bottom lines represent the 25th and 75th percentiles, respectively, while the whiskers extend to the highest and lowest values within 1.5 times the interquartile range. The middle line of each boxplot indicates the median.

4.2.3 Evolution of permafrost thermal conditions

Figure 10 shows ~~presents~~ the simulated interdecadal changes in ~~time series of spatial snapshot relative changes in interdecada~~l MAGT15m, TTOP, and ALT across the WKL permafrost survey region for 1980–2022. From the 1980s to the 1990s, the modeled MAGT15m remained relatively stable in 62.40% of the region (±0.3°C; Fig. 10a) ~~across most of the WKL region (62.40%)~~

~~exhibited relatively small variability, ranging from -0.3°C to 0.3°C (Fig. 10a).~~ A clear warming trend prevailed from the 1990s to the 2000s, with the modeled MAGT15m increasing in 67.20% of the region, and the highest modeled values exceeding 1.8°C in certain local areas (Fig. 10b). ~~From the 2000s to 2010–2022, the warming trend showed more pronounced fluctuations, with some areas even experiencing cooling compared to the previous decade. However, during this period, about 47.10% of the region experienced a cooling trend, with the largest decrease in MAGT15m reaching up to -1.8°C (Fig. 10c).~~ From the 2000s to 2010–2022, warming became more variable, and 47.1% of the region experienced cooling, with decreases up to −1.8°C (Fig. 10c). Overall, from 1980 to 2022, 58.6% of the region warmed (up to +1.8°C), while 25.5% mainly in central WKL cooled, with decreases below −1.8°C (Fig. 10d).~~during the simulation period from 1980 to 2022, the MAGT15m for most of the WKL permafrost survey region (58.58%) shows a warming trend, with increases ranging from 0.01°C to 1.8°C. Meanwhile, approximately 25.50% of the central region displays a noticeable cooling trend, with the most pronounced decreases modeled below -1.8°C (Fig. 10d).~~

TTOP followed a ~~S~~similar trend~~ly~~, The largest increase occurred between the 1990s and 2000s, when 86.7% of the region warmed, and 16.4% showed increases above 0.8°C (Fig. 10e). ~~across different decades, the most pronounced increase in TTOP occurred between the 1990s and 2000s, with 86.66% of the region experiencing a warming trend, and 16.35% of the area showing a warming magnitude exceeding 0.8°C. Following this,~~ F~~f~~rom the 2000s to 2010–2022, ~~about~~ 70.46% of the area experienced a warming trend, with increases ranging from 0.1°C to 1.8°C (Fig. 10e-g). ~~According to the modeled TTOP outputs for the period from 1980 to 2022, approximately 81.68% of the area displayed an increasing trend, with about 17.20% of regions showing a warming magnitude above 1.3°C. However, in a small area (about 7.42%) located in the central part of WKL, the simulated TTOP showed a drastic decrease, ranging from -0.3°C to -1.3°C (Fig. 10h).~~Over the full period, 81.7% of the region experienced a TTOP increase, with 17.2% warming by over 1.3°C. However, a small central area (~7.4%) showed declines ranging from −0.3°C to −1.3°C (Fig. 10h).

~~For~~ ALT increased ~~, the~~ most pronounced increase between the ~~was simulated across WKL from the~~ 1980s and ~~to~~ the 1990s, with 74.20% of the region experiencing an increase ranging from 0.1m to 1.5m, and in some areas, even exceeding 1.5 m during this period (Fig. 10i). ~~Following this, f~~From the 2000s to 2010–2022, approximately 59.0% of the region experienced ~~an increase in ALT, in which 6.14% of area shown a pronounced increase ranging from 0.3m to 1.5m. Meanwhile, approximately 0.97% of the area experienced a drastic decrease in ALT, with reductions exceeding -0.8m during the same period (Fig. 10k).~~ 59% of the area experienced ALT increases, while 0.97% showed sharp declines beyond −0.8 m (Fig. 10k).. ~~However, compared to the previous decade, a slowdown in ALT increase was observed from the 1990s to the 2000s, with 58.0% of the region~~

~~experiencing a modeled ALT increase (Fig. 10j). Notably, during this period, approximately 7.61% of the region experienced a noticeable decline in ALT, with reductions ranging from -0.3m to -1.0m.~~ Overall, ALT increased by an average of 0.17 m across WKL from 1980 to 2022, ~~the average ALT in WKL increased by 0.17m~~, with 83.10% of the region exhibiting increasing trend, ~~and the highest increases exceeding 1.5m. Meanwhile, approximately~~and 16.90% mainly central cooling, in some places by more than −0.8 m (Fig. 10l). ~~of the central region experienced a decline in ALT, ranging from -0.1m to -0.8m, with the most pronounced reductions locally exceeding -0.8m (Fig. 10d).~~

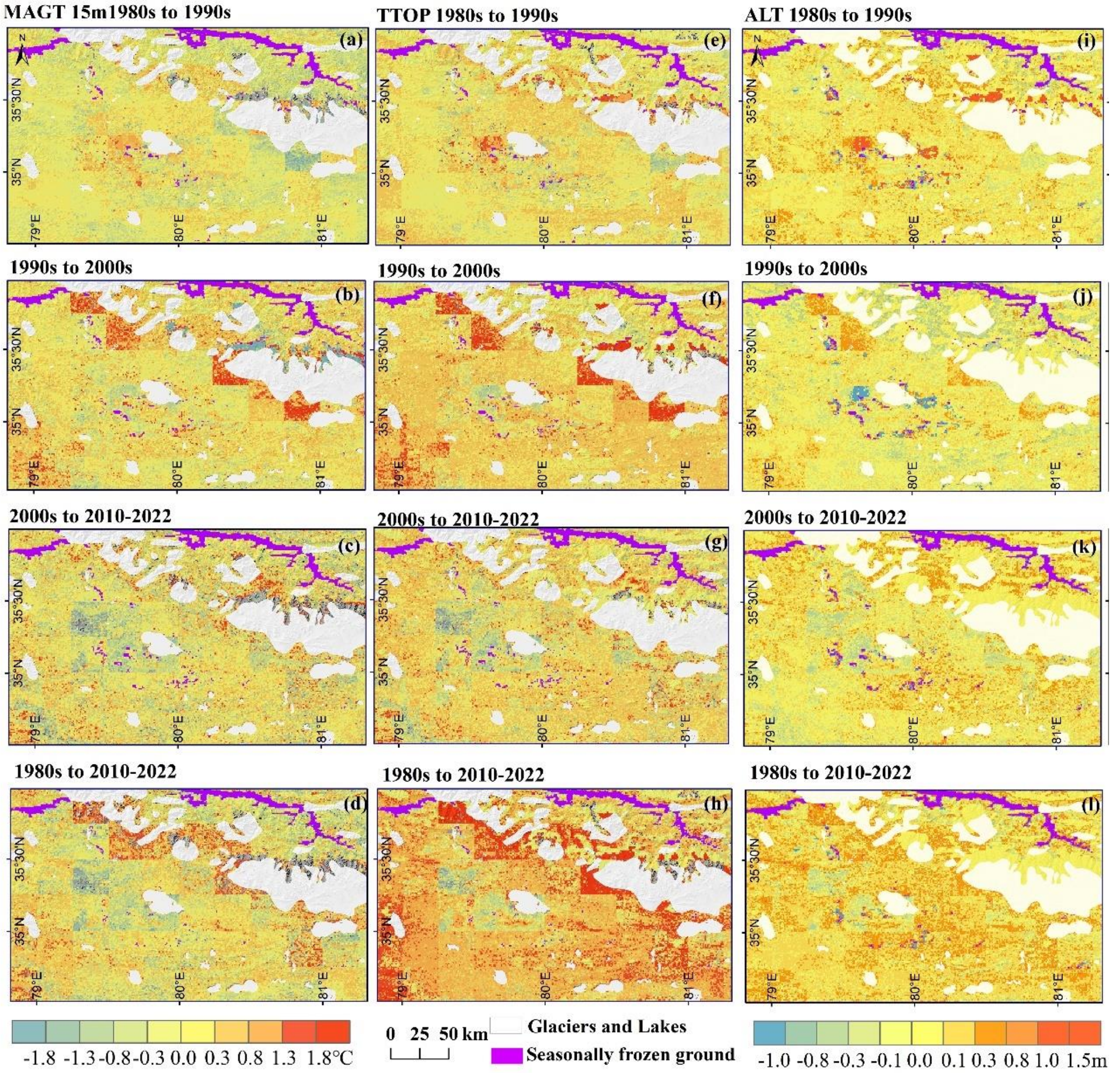

Figure 10: Spatial relative changes in the modeled MAGT15m (left column: a-d), TTOP (middle column: e-h), and ALT (right column: i-l) for the decades of the 1980s, 1990s, 2000s, and the period from 2010 to 2022. Seasonally frozen ground is depicted in purple, while glaciers and lakes are shown in grey.

Figure 11 illustrates the interdecadal variations ~~characteristics~~ of MAGT15m, TTOP, and ALT across different elevations zones and soil stratigraphic classes. Overall, ~~The~~the ~~results indicate that the~~ modeled MAGT15m exhibited relatively small interdecadal variations and a slight overall increase from the 1980s to 2010-2022. The most noticeable increase occurred at the highest elevations (5600–6000 m a.s.l.), though changes remained less pronounced than those in TTOP (Fig. 11a–b). MAGT15m showed no significant differences across soil classes (Fig. 11d). ~~During the simulation period, the most distinct changes in modeled MAGT15m occurred in the highest elevation range (5600-6000 m a.s.l.), which showed an upward trend over time. However, the magnitude of these changes was less intense compared to those simulated in the simulated TTOP (Fig. 11a-b). Furthermore, the interdecadal changes in MAGT15m did not show apparent discrepancies across different soil stratigraphic classes (Fig. 11d)~~. In contrast, TTOP exhibited a clear warming trend ~~was observed in the modeled TTOP~~ across various soil stratigraphic classes, ~~with the~~ exception of the alluvial sedimentary class. ALT ~~As for ALT, the simulated values~~ showed a remarkable increasing trend across various elevation ranges from the 1980s to the 2000s). (Fig. 11c)~~. Furthermore, the modeled ALT values~~ and exhibited high interdecadal variability across different soil stratigraphic classes. The largest ALT increase (>0.17 m) simulated in ~~In the~~ alluvial and lacustrine sediment classes, while the smallest (0.11 m) was ~~the modeled ALT showed a substantial increase from the 1980s to 2010–2022, with an increase exceeding 0.17 m. In contrast, the smallest change, an increase of 0.11 m, was simulated~~ in the glarosion sediment class (see Fig. 1f)~~.~~

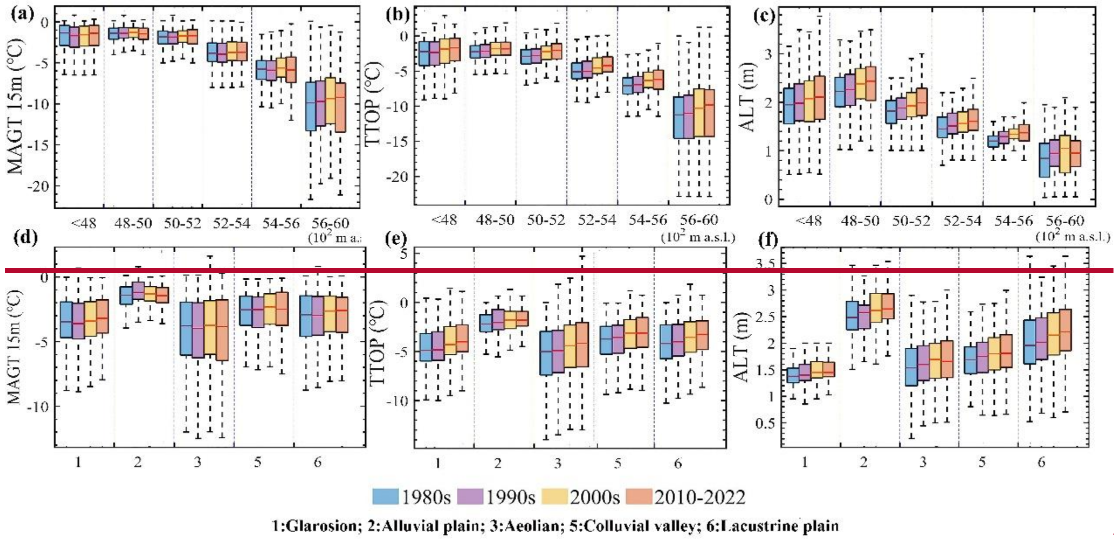

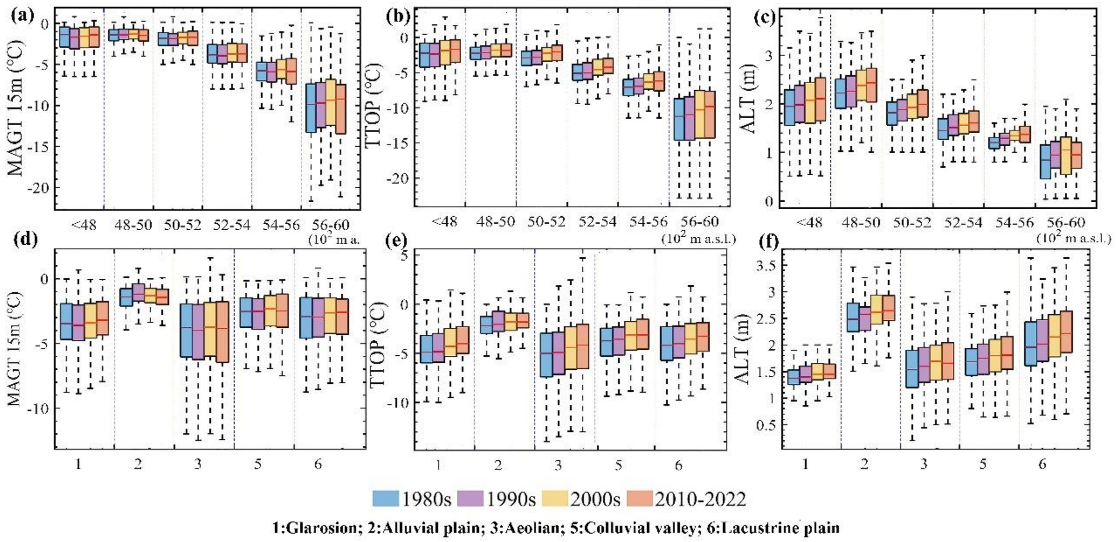

Figure 11: Boxplot maps of modeled MAGT15m (first column: a,d), TTOP (middle column: b,e), and ALT (right column: c,f) for four period (1980s, 1990s, 2000s, and 2010-2022, depicted in different colored boxes). The data is categorized by different elevations (ranging from 4300 m a.s.l. to 6000 m a.s.l.) in the first row, and by soil stratigraphic classes—Glarosion, Alluvial plain, Aeolian, Colluvial valley, and Lacustrine—in the bottom row. The top and bottom lines of the boxplots represent the 75th and 25th percentiles, respectively. The whiskers extend to the highest and lowest values within 1.5 times the interquartile range. The middle line of each boxplot indicates the median.

4.2.4 Evolution of permafrost extent

Table 3 shows the permafrost aggradation and ~~/~~degradation in response to climate variability ~~during the 1980-2022~~ across the WKL permafrost survey area from 1980 to 2022. According to the initial simulation outputs from the 1980s, approximately 82.27% of the total area in WKL was underlain by permafrost. Of this, 55.58% was found in areas classified as Aeolian ground stratigraphy, and 67.9% was located at elevations ranging from 4800 to 5600 m a.s.l.

Throughout the study period, the number of grid cells with simulated permafrost extent remained unchanged from ~~constant~~ between the 1980s and 1990s. A slight decline of 0.15% was simulated between the 1990s and 2000s, followed by a 0.44% increase from the 2000s to 2010–2022. These changes were primarily concentrated in low-elevation areas below 4800 m a.s.l. and in regions with alluvial plain sediments (Table 3).~~However, from the 1990s to the 2000s, a modest reduction of 0.15% in permafrost areas was modeled, followed by a 0.44% increase between the 2000s and 2010–2022. Spatially, most of these changes occurred in low-elevation regions below 4800 m a.s.l. and in areas classified as Alluvial plain sediments (Table 3).~~ Overall, the simulations indicate that permafrost extent in WKL has remained relatively stable over the 43 years ~~results suggest a relatively stable permafrost extent in WKL over the past 43 years.~~

Table 3. ~~Variations~~ Change in the areal extent of frozen ground types across the WKL permafrost survey region from 1980 to 2022, ~~. The data is~~ categorized by elevation and soil stratigraphic classes.

Altitude range $(10^2 m\ a.s.l)$	Permafrost areal extent (%)								SF. (%)
	<48	48-50	50-52	52-54	54-56	56-60	>60	Sum	
1980s	**2.74**	12.58	18.79	24.32	12.22	9.07	2.56	82.27	2.67
1990s	**2.87**	12.48	18.76	24.32	12.22	9.07	2.56	82.27	2.67
2000s	**2.84**	12.46	18.67	24.31	12.22	9.07	2.56	82.13	2.81
2010-2022	**3.01**	12.62	18.78	24.32	12.22	9.07	2.56	82.57	2.36
Stratigraphic class	1	2	3	5	6				
1980s	12.32	**5.92**	55.58	3.51	4.95			82.27	2.67
1990s	12.36	**5.75**	55.71	3.51	4.94			82.27	2.67
2000s	12.36	**5.70**	55.62	3.51	4.95			82.13	2.81
2010-2022	12.34	**5.81**	55.94	3.51	4.97			82.57	2.36

Note: SF. indicates seasonally frozen ground. The numbers for soil stratigraphy correspond to the following sediment classes: 1: Glarosion; 2: Alluvial plain; 3: Aeolian, 5: Colluvial valley, and 6: Lacustrine. The glacier and lake area, accounting for 15.06%, was excluded from this statistic. Mainly changes are shown in bold.

5 Discussion

5.1 Applicability of the forcing data

~~Most previous evaluations indicated that soil temperature products derived from atmospheric circulation models or ESMs, which typically have coarse resolutions (~300 km), show larger uncertainties over the QTP, particularly permafrost region (Hu et al., 2019; Qing et al., 2020; Yang et al., 2020; Xi et al., 2023). At such resolutions, model forcing may not accurately represent permafrost thermal conditions due to the strong spatial variability of soil temperature and active layer thickness, driven by surface cover and soil moisture heterogeneity on the QTP (Hu et al., 2023). These inaccuracies in model forcing directly affect the accuracy of thaw depth simulations, often leading to an overestimation of permafrost degradation rates, which is inconsistent with current~~

~~observed patterns (Lawrence et al., 2012; Zhao et al., 2024). In this study, we applied machine learning techniques to reconstruct remote-sensing-based land LST back to 1980 with a spatial resolution of 1 km and a monthly temporal resolution based on field observations, satellite data, and reanalysis products. Compared to in situ measurements, we found a slight cold bias in our reconstructed LST series, averaging approximately -0.80°C, particularly during summer months (see details in Sect. 3.1). This bias may be attributed to residual biases in the LST_Zou dataset, which exhibits a noticeable cold bias during these months. Nevertheless, the reconstructed thermal state of permafrost achieved an accuracy of ±0.25°C at 10 m depth, and active layer thickness (ALT) was reproduced within ±0.25 m—an improvement over previous studies that used coarser atmospheric forcing in similar domains (e.g., Chen et al., 2015; Wu et al., 2018). This confirms the appropriateness of the models to accurately simulate the permafrost thermal reges over long time scales.~~

~~Additionally, our analysis showed that the WKL permafrost survey area has experienced pronounced LST warming since the mid-1980s, with an accelerated warming trend in the last decade. This pattern aligns well with the documented warming trends on the QTP in recent studies (Jin et al., 2011; You et al., 2021; Yao et al., 2021; Li et al., 2024), indirectly validating the accuracy of our reconstructed LST data. Overall, we conclude that, compared to traditional atmospheric forcing, this new model forcing is a suitable choice for modeling ground thermal regime dynamics over the WKL. It enables simulations of the permafrost thermal state with a much higher degree of precisions and spatial resolution than traditional model forcing, which is consistent with previous findings (Zhao et al., 2022). Similar findings suggest that enhancing the spatial resolution of the forcing dataset can greatly improve the accurate representation of the effects of varying subsurface and surface properties on ground temperatures and thermal modeling accuracy (e.g., Zhang et al., 2013; Fiddes et al., 2015).~~

Previous studies have shown that coarse-resolution soil temperature products from atmospheric reanalysis datasets—such as ERA-Interim (0.125° × 0.125°) and ERA5-Land (0.1° × 0.1°)—as well as assimilated products like the Chinese meteorological forcing dataset CLDAS (0.0625° × 0.0625°), exhibit substantial uncertainties when applied to the QTP, particularly in permafrost regions (Hu et al., 2019; Qing et al., 2020; Yang et al., 2020). At these spatial scales, the forcing data often fail to capture the complex heterogeneity in surface cover and soil moisture that drives spatial variability in ground temperature and ALT across the QTP (Hu et al., 2023). These limitations contribute to large uncertainties in simulating permafrost thaw depth and often result in degradation rates that deviate from observed trends (Lawrence et al., 2012; Zhao et al., 2024).

In contrast, satellite remote sensing products such as MODIS LST offer higher spatial resolution and long-term regional coverage, and can potentially better capture surface heterogeneity, thereby reducing modeling uncertainties. However, MODIS LST has several limitations for permafrost modelling applications: it measures the skin temperature rather than the true ground surface temperature, often reflecting the surface temperature of vegetation canopies or snow. Additionally, snow cover introduces thermal insulation effects, cloud cover leads to data gaps, and only clear-sky conditions are captured.

To address these challenges, we used a modified LST product developed by Zou et al. (2017), which incorporates cloud-gap filling and calibration with ground-based AWS observations to better account for surface heterogeneity. Validation at three typical permafrost sites in the central permafrost zone and the WKL region demonstrated strong performance. In our study, this product was further improved using a machine learning approach to reconstruct pre-2003 LST by integrating multiple data sources. The reconstructed LST outperformed the original product slightly ($R^2 > 0.95$, MAE = 1.29–1.50°C, RMSE = 1.62–1.91°C), and showed significant improvement over ERA5-Land LST.

While direct validation of pre-2003 LST is not possible due to the lack of satellite or ground observations in the WKL region. We employed an indirect validation approach: the reconstructed LST was used to force the MVPM to simulate permafrost thermal dynamics from 1980 onward. The simulation results were evaluated against existing permafrost monitoring data and previously published permafrost distribution maps from various periods, i.e.1980s (Li et al., 1996), 2000s (Wang et al., 2006), 2010 (Cao et al., 2023), and post-2010 (Zou et al., 2017). The strong agreement between the MVPM outputs and these independent sources supports the reliability of the pre-2003 LST reconstruction. Moreover, our analysis reveals pronounced LST warming in the WKL survey area since the mid-1980s, with accelerated warming over the last decade. This trend aligns with recent documented warming across the QTP (Jin et al., 2011; Yao et al., 2019; You et al., 2021; Li et al., 2024), providing further indirect validation of the reconstructed LST. Collectively, this multi-faceted validation approach provides reasonable confidence in our LST dataset, despite the lack of direct early-period observations. While we acknowledge this limitation, we believe our methodology offers a robust solution given the data constraints of this remote and observationally challenging region.

The above comparisons show that the reconstructed LST closely aligns with in situ data and is suitable for ground thermal modeling. However, a seasonal cold bias remains, especially in July–

September (Figure 3), leading to a slight underestimation of shallow soil temperatures, resulting in a cold bias in ALT. Such bias is likely due to the sensitivity of near-surface ground temperature to seasonal forcing. Similarly, Westermann et al. (2015) found that an LST uncertainty of ±2 °C can lead to a ±3 cm uncertainty in simulated thaw depth. We conducted a sensitivity analysis (Figure 12) to evaluate the impact of uncertainties in model forcing (e.g., LST) on simulation results, and the findings confirm the model's robustness to LST biases. Moreover, since thermal signals attenuate with depth and ground temperatures at the ZAA level reflect long-term trends (Jin et al., 2011; Dobi ński et al., 2022), the observed cold bias appears to be seasonal and has limited influence on long-term permafrost dynamics.

Nonetheless, in complex mountainous terrain, a 1 km grid cell is insufficient to capture micro-topographic features such as slope, aspect, and wind-driven snow redistribution—factors that strongly influence local permafrost hydrothermal dynamics. Therefore, our modeling scheme should be considered as a first-order approximation of permafrost thermal distribution, rather than a tool for detailed slope-scale assessments in these areas. In addition, resampling coarse-resolution input datasets to match the model resolution introduces uncertainties in the LST reconstruction process. Despite these limitations, the model successfully reproduces regional permafrost thermal patterns in the WKL area, as confirmed by in situ observations and existing permafrost maps. Although constrained by the spatial resolution of satellite-derived LST, the approach performs well in simulating the thermal state and ALT of permafrost, providing valuable insights for remote, data-scarce regions of the western QTP. Future improvements will require the integration of higher-resolution datasets and enhanced representation of sub-grid variability.

~~5.2 Spatiotemporal variations in thermal responses to climatic variability~~

5.2 Permafrost thermal stability and warming trends

~~In this study, we investigated the spatiotemporal dynamics of the permafrost thermal regime in response to climate variability from 1980 to 2022 in a representative permafrost region on the northwest QTP (WKL). We found that the most drastic permafrost thermal warming (MAGT15m and TTOP) was modeled between the 1990s and 2000s, which does not correspond to the periods of the strongest warming in LST, observed during the 1980s and warming accelerated last from 2010. However, ALT variations were more consistent with LST fluctuations, and the most pronounced increase in ALT was modeled between the 1980s and 1990s. Similar warming effects on ALT have been observed in the QTH (Li et al., 2012), where observed variations in ALT are primarily influenced by seasonal air temperatures and shallow ground temperatures, and thus exhibit inter-annual variation. Furthermore, our simulation indicated that the TTOP responded more rapidly~~

~~and experienced more pronounced warming from 1980 to 2022. These phenomena can be explained that changes in TTOP are characterized by short time lags in relation to ground surface temperature fluctuations, along with large amplitudes and high rates of temperature increase (Wu et al., 2010). Thus, the response of near-surface ground temperature to changing climate forcing is fast to immediate. In comparison, due to the exponential attenuation of heat transfer with depth, the amplitudes (seasonal variations) and rates of temperature increase diminished, resulting in longer time lags at the depth of zero annual amplitude (Jin et al., 2008, 2011; Noetzli et al., 2009). Consequently, relatively stable thermal conditions were modeled for the MAGT15m during the same period.~~

~~Spatially, the characteristics of permafrost thermal warming vary widely across the study area and are strongly dependent on its initial thermal state. The magnitude of change was relatively low, typically less than ±0.3°C, in transitional (−1.5°C < MAGT15m < −0.5°C) and unstable (−0.5°C < MAGT15m < 0.5°C) permafrost. In contrast, the most pronounced warming in MAGT15m was modeled in stable permafrost (e.g., MAGT15m<−1.5°C), with warming magnitudes reaching up to 1.8°C, and some localized areas experiencing even greater increases. This changing pattern generally exhibits an obviously altitude-dependent in spatial distribution characteristic. A similar permafrost thermal warming pattern has been observed in the QTH and Arctic regions, including Alaska and Russia (Smith, 2022; Zhao et al., 2020). This occurs because when cold permafrost is warms, its temperature initially rises. However, as the permafrost temperature approaches the thawing point (e.g., 0°C), ground ice begins to melt over a range of sub-zero temperatures. This phase change absorbs a large amount of heat, resulting in lower apparent thermal diffusivity and less energy directed toward increasing ground temperature (Langer et al., 2013, 2024). Consequently, under similar external conditions, stable permafrost experiences relatively higher warming rates and amplitudes.~~

~~However, what is more noteworthy is that, although the increase in permafrost temperature within unstable and transitional zones was smaller, slower, and less sensitive to climate warming, ground ice melt will lead to permafrost degradation. This degradation will convert permafrost into seasonally frozen ground, subsequently inducing substantial geomorphic changes, such as ground surface subsidence or hillslope failures, which result in challenges for engineering and natural hazard prediction and mitigation. As shown in our simulation results, there was a change in permafrost extent across the WKL, particularly in low-elevation regions below 4800 m a.s.l., where the MAGT was greater than −0.5°C, especially in permafrost boundary areas near the thawing point (0°C). Thus, regions with the least warming modeled may still be the most susceptible to permafrost~~

~~degradation in response to climate warming. Unlike the spatial characteristics of changes in the thermal state of permafrost, which are almost entirely governed by elevation, the simulated variations in ALT are influenced not only by elevation but also significantly by ground stratigraphy. The highest average ALT of 2.5 m was modeled in the alluvial sediments class, showing a substantial increase during the simulation period, whereas the lowest ALT of 1.5 m was modeled in the glarosion sedimentary class, with a relatively minor increase over the same period. Similar patterns of ALT changes have also been simulated in circumpolar Arctic permafrost regions (Langer et al., 2013; Westermann et al., 2015).~~

Permafrost thermal degradation is a complex process marked by a delayed response to climate warming and influenced by local environmental factors such as soil type, ground ice content, geothermal heat flux, and the initial thermal state of the permafrost (Zhao et al., 2020; 2024; Hu et al., 2023). In response to climate change, permafrost gradually adjusts its thermal regime over multiple timescales, ranging from years to centuries or even millennia. Based on ground temperature profile classifications, Wu et al. (2010) proposed that the current diversity in permafrost thermal conditions across the QTP may reflect different stages of degradation—such as the warming stage, zero geothermal gradient stage, talik development stage, and complete disappearance—tracing back to the cold climatic conditions of the Last Glacial Maximum (LGM).

In this study, we examined the spatiotemporal dynamics of permafrost thermal regimes in response to climate variability from 1980 to 2022 in a representative region of the northwestern QTP, i.e. the WKL permafrost survey area. Our simulation results show that approximately 70.98% of permafrost in this region is currently in a temperature-rising stage, characterized by an initial MAGT below –2.0 °C and an ALT of less than 1.5 m, mostly occurring at elevations above 4800 m a.s.l. Another 17.58% is transitioning toward the zero geothermal gradient stage, while only 11.44% is either in that stage or progressing toward talik development. These latter types are generally found at lower elevations (below 4800 m a.s.l.) and are associated with relatively high MAGT values (above –1 °C), suggesting ongoing degradation.

Permafrost forms when long-term ground surface heat loss exceeds incoming heat under persistently cold climate conditions (Wu et al., 2010). In a warming climate, sustained increases in surface temperature disturb the previous thermal equilibrium, leading to excess heat accumulation in the active layer. This causes progressive ground warming from the surface downward and reduces the vertical thermal gradient within the permafrost. Notably, during the early stages of warming, permafrost temperatures rise more quickly than thaw occurs, as much of the energy is used to warm the frozen soil to its thaw point. This explains why the overall areal extent of permafrost in the WKL remained relatively stable during the simulation period, despite a pronounced warming trend. Interestingly, while regional average LST showed a steady increase from 1980 to 2022, considerable interannual and spatial variability was observed. We hypothesize that intermittent cooling episodes may have triggered the formation or re-expansion of permafrost in certain areas through delayed responses—a view supported by our simulation, which showed a slight increase in permafrost extent between 2010 and 2022 despite continued warming.

Looking ahead, under continued climate warming, MAGT is expected to increase further. As heat penetrates deeper into the ground, the thermal gradient at the base of the permafrost eventually drops below the geothermal gradient, causing heat to flow upward from the unfrozen substrate. This initiates basal thaw, leading to a gradual upward retreat of the permafrost base and overall thinning of the permafrost layer. Due to its relatively high geothermal gradient, the QTP shows a slower thermal response to atmospheric warming than Arctic and sub-Arctic regions (Jin et al., 2011), resulting in lower rates of ground temperature increase (Zou et al., 2017).

As permafrost temperatures approach 0 °C, ground ice near the permafrost table begins to melt, absorbing large amounts of latent heat, a phenomenon known as the “zero curtain effect.” This process significantly slows or even temporarily halts further warming and reduces seasonal temperature fluctuations in the shallow permafrost. Meanwhile, geothermal heat from below is largely consumed by thawing permafrost from the bottom up. The zero geothermal gradient stage represents a critical transitional phase, in which nearly all surface heat is devoted to ice melt. Once seasonal freezing no longer reaches the permafrost table, a talik—an unfrozen zone within permafrost—forms and expands. Numerical simulations by Sun et al. (2019) suggest that talik formation accelerates thaw and marks the onset of irreversible degradation, continuing until complete permafrost loss.

However, the entire permafrost degradation process tends to be slow and delayed. Previous assessments have shown that permafrost loss, especially in terms of areal extent, does not follow a linear trend, and that temperature responses to climate warming occur more slowly than suggested in many earlier studies (Guo et al., 2012; Ni et al., 2021). Even under the extreme RCP8.5 scenario, simulations project only gradual deepening of the permafrost table. For example, by 2050, permafrost is still expected to persist at a depth of 40 m at Wudaoliang and Tanggula—two borehole sites in the continuous permafrost zone, where ground temperatures are cold and permafrost layers are thick. In contrast, at Xidatan, located near the lower boundary of the permafrost zone with a warmer, thinner (~32 m) permafrost layer, the permafrost base is projected to retreat more significantly. Nevertheless, simulations suggest permafrost will still exist at this site through 2100, based on trends in deep ground temperature, ice content, and thermal gradients. Similar results have been reported for the northern margin of the QTP permafrost zone. MVPM-based modeling (Zhao et al., 2022) shows that MAGT will continue to rise under gradual warming. Warming rates are projected to be slightly higher under Shared Socioeconomic Pathways (SSPs) than under Representative Concentration Pathways (RCPs), although no major differences are projected in terms of areal permafrost extent. These findings indicate that, while permafrost temperatures are increasing, the rate of spatial loss remains relatively slow, an insight critical for modeling the magnitude and timing of permafrost carbon feedbacks and associated hydrological processes.

It is also important to recognize that the thermal response of permafrost to warming may vary considerably in ice-rich zones, particularly those with excess ground ice. In such areas, thawing of massive ground ice and associated water dynamics significantly shape degradation trajectories, often leading to landscape changes such as surface subsidence and thermokarst pond formation (Westermann et al., 2016). These hydrological feedbacks can either slow or accelerate thaw. Efficient drainage of meltwater delays talik development and surface collapse (Westermann et al., 2016), while surface water accumulation promotes heat transfer and deeper thawing (Jan et al., 2020). These processes increase the potential release of vast stores of frozen organic carbon—particularly CO_2 and CH_4—trapped in cold, ice-rich lowlands. Therefore, thermokarst-driven permafrost degradation under continued warming could greatly amplify the global permafrost carbon–climate feedback (Turetsky et al., 2015).

5.3 Comparison with previous studies

~~It is well recognized that global-scale warming has impacted the thermal regime of permafrost worldwide; however, it is still not fully understood how, at what rate, and to what extent permafrost responds to climate fluctuations. This is partly because permafrost thermal dynamics are generally poorly represented in global models, particularly in complex regions such as the QTP, leading to huge uncertainties in predicting permafrost thermal state responses and climate feedbacks. In this study, we used the MVPM to simulate thermal state in the WKL region in response to climate change from 1980 to 2022. We quantified the spatial changes in permafrost and seasonally frozen ground across the WKL region during the simulation period (1980–2022). The model outputs are compared with published maps from four different periods (see details in Fig. 9). Overall, most of the simulated~~

~~permafrost distribution aligns with existing maps. However, notable differences occur in areas of seasonally frozen ground, similar to the permafrost distribution modeling conducted by Zhao et al. (2022) in the Xidatan region of the QTP. These discrepancies may result from variations in model forcing, models, study periods, spatial resolution, and other local factors (Zhao et al., 2022; Zou et al., 2017). The maps by Li and Cheng (1996) and Wang et al. (2006) synthesize available field data for permafrost occurrent and properties, literature, aerial photographs, satellite images, and other sources. In these maps, permafrost boundaries were primarily determined using air temperature or mean annual ground temperature (MAGT) isotherms as thresholds and were manually delineated on topographic maps at scales of 1:3,000,000 and 1:4,000,000, respectively (Cao et al., 2016). The manual cartographic techniques used to delineate permafrost boundaries are prone to artifactual errors, inevitably introducing uncertainties in the maps by Li and Cheng (1996) and Wang et al. (2006). Additionally, the coarse resolution of these maps does not adequately capture fine-scale variations in ground conditions, making it difficult to validate the results against field observations.~~

~~In contrast, the maps by Cao et al. (2023) and Zou et al. (2017), as well as our simulation outputs, are based on enhanced remote-sensing LST products with a spatial resolution of 1 km. These maps show higher accuracy in identifying both permafrost and seasonally frozen ground compared to borehole observations. Moreover, the results reveal more spatial details. This finding underscores the potential advantages of remote sensing methods for studying regional-scale permafrost thermal regimes on the QTP, as noted by Zhao et al. (2022). The differences arise primarily because the maps by Cao et al. (2023) and Zou et al. (2017) assume that permafrost is in equilibrium with long-term climate conditions—specifically, averaging the periods from 2005 to 2010 for Cao et al. (2023) and 2003 to 2012 for Zou et al. (2017). In reality, ground temperature observations and modeling studies have shown that the permafrost conditions are not in equilibrium with the atmospheric climate. Additionally, these maps do not account for the thermal state of deep permafrost, as the modeled soil column typically extends to depths less than 3 m. In the meantime, as supra-permafrost subaerial taliks exist in some areas, the criterion of subzero TTOP used in Cao et al. (2023) and Zou et al. (2017) for determining permafrost occurrence may underestimate the extent of permafrost. Consequently, the areal extent of permafrost distribution estimated in these equilibrium-based maps is likely slightly underestimated compared to our simulation outputs (Zhao et al., 2022).~~

~~Compared to the equilibrium approach of Cao et al. (2023) and Zou et al. (2017), we employed a numerical model, that can simulate the transient changes in ground temperature and the spatial extent of permafrost distribution under climate change. Our modeling output suggests that the~~

~~original thermal condition of permafrost over the WKL is relatively cold, with 80% of MAGT15m ranging from −7.5°C to −1.5°C. Of this, 34.13% corresponds to very stable permafrost (MAGT < −5°C), 22.12% to stable permafrost (−5°C < MAGT < −3°C), and 23.08% to sub-stable permafrost (−3°C < MAGT < −1.5°C). In response to climate changes from 1980 to 2022, permafrost areal extent distribution in the WKL remained relatively stable, with less than 0.5% of permafrost experiencing aggradation or degradation due to climate fluctuations during this period. These results align well with borehole observations (Jin et al., 2011), which indicate that permafrost is more thermally stable in continental climate regions influenced by stronger westerlies, particularly in the interior, as well as in the western and northern areas of the QTP, including the WKL. However, some studies report contrary findings, suggesting a faster response of permafrost to climate change (Guo and Wang et al., 2012, 2016; Ni et al., 2021; Shen et al., 2023). This discrepancy is largely due to model deficiencies that fail to capture the time lag between climate warming and permafrost thawing in areas with thick permafrost. These limitations often stem from scarce observational data and an incomplete understanding of the complex physical processes in permafrost on the QTP (Sun et al., 2019; Hu et al., 2023). Most simulations of hydrothermal processes focus on shallow layers, and changes in heat and moisture within frozen soil are often ignored, hindering accurate predictions of heat and water exchanges in permafrost under climate change (Hu et al., 2023).~~

~~Moreover, permafrost on the QTP developed over a prolonged period of cold paleoclimate, resulting in a ground thermal state characterized by low temperatures and ground ice (Jin et al., 2011; Zhao et al., 2020). Current ground temperatures at various depths reflect cumulative historical climate changes, especially in deeper soil layers (i.e., tens to hundreds of meters) (e.g., Lachenbruch and Marshall, 1986; Allen et al., 1988; Osterkamp and Gosink, 1991; Harrison, 1991; Buteau et al., 2004; Kneier et al., 2018; Langer et al., 2024). Therefore, the initial thermal state of permafrost, shaped by past climates, is essential for accurately simulating permafrost's thermal responses to climate warming. However, many numerical models often overlook the historical energy accumulated in permafrost and the effects of ground ice conditions below a depth of 1 m (Zhao et al., 2020; Hu et al., 2023). Furthermore, many models simplify the geothermal heat flux by setting a zero-flux or constant-temperature condition at the bottom boundary (Wu et al., 2010; Xiao et al., 2013, Zhao et al., 2022). This potentially omits critical factors in long-term permafrost evolution and introduces large uncertainties in modeling both the present state and projected changes in permafrost temperature. Another limitation is that most current models do not account for the thaw settlement process. As ground ice thaws, it causes settling and consolidation of ground material, potentially leading to an underestimation of permafrost thawing, as the permafrost table may be closer to the ground surface than predicted. This omission can also introduce errors in simulating~~

~~ALT and the burial depth of the permafrost table (Sun et al., 2023).~~

~~In comparison, our model fully accounts for the thermal-property differences between frozen and thawed soil, phase changes of unfrozen water in frozen soil, ground ice distribution, thaw settlement, and geothermal heat flow. The modeled ground temperature, ALT, thaw depth, and permafrost distribution align well with observations, indicating that the MVPM accurately simulates the heat transfer process in permafrost and effectively captures the attenuation and time lag of heat transfer in deep permafrost. Notably, most numerical models overlook the thermal properties and processes in deeper permafrost, while our findings emphasize that these factors play a critical role in permafrost evolution and thaw trajectories in response to climate change.~~

It is well recognized that global warming has significantly influenced the thermal regime of permafrost worldwide. However, the mechanisms, rates, and extent of permafrost responses to climate fluctuations remain poorly understood. This is partly due to the inadequate representation of permafrost thermal dynamics in global models, especially in complex regions like the QTP, resulting in large uncertainties in simulate of permafrost change and associated climate feedbacks. In this study, we used the MVPM framework to simulate permafrost thermal states in the WKL region from 1980 to 2022 under changing climate conditions. Meantime, we quantified the spatial changes in permafrost and seasonally frozen ground over the simulation period. The model outputs were compared with four published permafrost distribution maps (see details in Fig. 9). Overall, the simulated permafrost distribution generally aligns with existing maps, although notable differences are observed in areas classified as seasonally frozen ground. Similar discrepancies were found in Zhao et al. (2022) for the Xidatan region of the QTP, likely due to differences in model forcings, model structures, study periods, spatial resolutions, and local environmental factors (Zhao et al., 2022; Zou et al., 2017).

The maps by Li and Cheng (1996) and Wang et al. (2006) were derived using field observations, literature reviews, aerial photos, satellite images, and other data sources. In these maps, permafrost boundaries were manually delineated based on air temperature or MAGT isotherms, using topographic maps at coarse scales of 1:3,000,000 and 1:4,000,000 (Cao et al., 2016). Manual cartographic techniques and low spatial resolution likely introduced significant uncertainties, limiting their utility in capturing fine-scale ground thermal variability or validating model outputs against field data. In contrast, the maps by Cao et al. (2023), Zou et al. (2017), and our simulation results rely on enhanced remote sensing LST products with a 1 km spatial resolution. These approaches yield higher accuracy in identifying both permafrost and seasonally frozen ground, and they provide greater spatial detail, aligning better with borehole observations. This highlights the advantages of remote sensing methods for studying regional-scale permafrost regimes on the QTP, as previously noted by Zhao et al. (2022).

However, the maps by Cao et al. (2023) and Zou et al. (2017) assume permafrost is in equilibrium with the long-term climate, averaging conditions over 2005–2010 and 2003–2012, respectively. In reality, ground temperature observations and numerical modeling show that permafrost is not in thermal equilibrium with the current atmospheric climate. Furthermore, these maps do not resolve deep permafrost conditions, as their models typically extend to depths of less than 3 m. In areas where supra-permafrost subaerial taliks exist, the subzero temperature at the top of permafrost (TTOP) criterion used in both studies may underestimate permafrost extent. As a result, these equilibrium-based maps likely slightly underestimate the areal extent of permafrost compared to our transient simulation results (Zhao et al., 2022).

Unlike the equilibrium-based approaches, our model simulates transient changes in ground temperature and permafrost extent in response to evolving climate conditions. Our results suggest that the permafrost extent in the WKL region remained relatively stable from 1980 to 2022, with less than 0.5% experiencing degradation or aggradation due to climate variability. These findings are consistent with borehole records (Jin et al., 2011), which indicate greater thermal stability of permafrost in continental interior regions of the QTP, particularly in the west and north where westerlies dominate.

However, some study report contrary findings, suggesting a faster response of permafrost to climate change (Guo and Wang, 2012, 2016; Ni et al., 2021; Shen et al., 2023), likely due to models that fail to capture the time lag between atmospheric warming and permafrost response in regions with thick permafrost. This discrepancy often stems from limited observations and an incomplete understanding of permafrost processes on the QTP (Sun et al., 2019; Hu et al., 2023). Many simulations focus on shallow soil layers and neglect coupled heat and moisture dynamics, limiting their accuracy in predicting long-term permafrost responses to climate change.

Permafrost on the QTP developed over millennia under cold paleoclimatic conditions, resulting in deeply frozen ground rich in ground ice (Jin et al., 2011; Zhao et al., 2020). Present-day ground temperatures at various depths reflect cumulative effects of historical climate variability, especially in deeper layers (e.g., tens to hundreds of meters) (Lachenbruch and Marshall, 1986; Allen et al., 1988; Buteau et al., 2004; Langer et al., 2024). Therefore, accurately modeling permafrost thermal dynamics requires realistic initial conditions that reflect this legacy. However, many models neglect the deep legacy energy and ground ice effects below 1 m depth (Zhao et al., 2020; Hu et al., 2023) and oversimplify geothermal heat fluxes, often applying zero-flux or constant-temperature bottom boundaries (Wu et al., 2010; Xiao et al., 2013; Zhao et al., 2022). These assumptions introduce major uncertainties in both present-day simulations and future projections.

To improve the long-term simulation of permafrost dynamics in ESMs, we recommend: i) Enhance lower boundary conditions by extending soil profiles to depths of 50–100 m and applying geothermal heat flux as the bottom boundary to better capture deep ground thermal processes; ii) Increase vertical resolution and improve model initialization—high-resolution vertical layering is crucial for resolving both seasonal and long-term temperature dynamics. Accurate initialization, including extended spin-up periods and calibration using in situ observations, is necessary to capture the thermal memory of deep permafrost; iii) Improve representation of ground ice processes by incorporating sub-grid scale variability, modeling the formation and melt of excess and segregated ice, and including thaw-induced surface changes such as thermokarst development; and iv) Use MVPM outputs to calibrate LSMs, employing high-resolution, observation-constrained simulations as benchmarks and leveraging satellite remote sensing data for parameter optimization and uncertainty reduction.

5.4 Current model shortcoming and future improvements

Model physics: Current MVPM configuration does not account for a range of processes that may influence the ground thermal regime in permafrost areas, such as non-conduction heat transfer due to soil water convection and the exchange of lateral heat or water fluxes. Previous studies have reported that lateral processes can significantly influence the ground thermal regime and contribute to the lateral degradation of permafrost. This has been confirmed by field investigations conducted at the margins of discontinuous permafrost zones and in areas around taliks, water bodies, and lakes (Boike et al., 2015; Bense et al., 2012; Sjöberg et al., 2016; Kurylyk et al., 2016). The impact of these local hydrological processes on permafrost thermal regimes remains unknown with the current model configuration. Thus, our simulations do not accurately represent areas with significant lateral heat fluxes, such as sharp mountain peaks, edges, or regions very close to water bodies. Despite these limitations, our model reasonably reproduces ground temperature and ALT, aligning well with observations in the WKL region. We believe that the dominant processes of permafrost heat transfer in the WKL permafrost survey region are effectively captured by the one-dimensional heat conduction approach.

In addition, the subsurface thermal model MVPM uses satellite-derived LST as the upper boundary condition, which does not explicitly account for snow and vegetation canopy effects, potentially introducing uncertainties in densely vegetated areas. However, in the permafrost regions of the QTP, snow cover is typically thin (~3 cm), short-lived (lasting less than a day per event), and vegetation is sparse, with less than 10% cover in the west (Wu and Zhang, 2008; Che et al., 2008; Wang et al., 2016; Zou et al., 2017; Yan et al., 2022). Under these conditions, the thermal offset between ground surface temperature (GST) and LST is minimal (Hachem et al., 2012). Our simulations reproduce observed MAGT and ALT well, supporting the validity of this approach for the region. While thin snow cover may briefly cool the surface due to high albedo and rapid melt (Zhang et al., 2005), this effect is likely negligible over the decadal timescale of our study. Still, the model's limitations highlight the need for further validation, especially regarding hydrogeological influences on permafrost thermal regimes and improved representation of surface heterogeneity in future developments.

~~In addition, the MVPM uses satellite-derived skin temperatures (i.e., LST) to define the upper boundary conditions, which do not account for the effects of vegetation canopies on ground thermal conditions and may introduce uncertainties in areas with dense vegetation. However, based on our field investigations, the vegetation in the WKL region is predominantly sparse alpine desert, with most areas being barren (Li et al., 2012; Wang et al., 2016; Zhao et al., 2019). This suggests that vegetation has a relatively limited effect on the estimated soil temperature. Nevertheless, the identified shortcomings suggest the need for further validation studies, particularly focused on hydrogeological processes impact on permafrost thermal regime, which will be a key focus for future work. Additionally, further model development is necessary to better represent surface heterogeneities.~~

Model initialization: ~~In this study, our model is initialized to an equilibrium condition using the forcing from the first year. This approach assumes that the initial permafrost regime was formed by land-atmosphere heat exchange under constant climate conditions for hundreds of years prior to 1980, which does not account for the transient nature of the ground temperature profile at that time. Although the impact of model initialization diminishes over time, grid cells where the initial forcing is near the threshold for permafrost occurrence remain strongly affected.~~

~~However, our model results provide a good reproduction of permafrost temperature, ALT, thaw depth, and four existing benchmark permafrost distribution maps across the WKL permafrost survey region. Based on this, we believe the uncertainties from model initialization should have a relatively limited effect on our long-term simulation results.~~

In this study, the model is initialized under equilibrium conditions using climate forcing from the first year, assuming that the permafrost regime prior to 1980 had been shaped by stable land–atmosphere heat exchange over several centuries. This approach does not capture the transient state of ground temperature profiles at that time. Although the influence of initialization decreases over time, grid cells with initial conditions near the permafrost thaw threshold remain more sensitive. Our sensitivity analysis shows that initial ground temperature has a moderate effect in seasonally frozen ground (~±0.12 °C), but a negligible impact in permafrost regions. These results indicate that the model reaches thermal stability during the simulation period. Furthermore, the model reliably reproduces observed permafrost temperatures, ALT, thaw depth, and aligns well with four benchmark permafrost distribution maps in the WKL survey region. Therefore, we conclude that uncertainties due to model initialization have a relatively minor effect on our long-term simulation outcomes.

~~*Ground thermal properties:* An accurate description of soil properties is essential for modeling water and heat processes in frozen soils at both global and regional scales (Dai et al., 2019; Lawrence and Slater, 2008; Harp et al., 2016; Hu et al., 2023). However, most soil datasets used in models are derived from seasonally frozen areas, while data coverage is extremely limited in the permafrost regions of the QTP, with significant gaps for deeper soil layers (Hengl et al., 2017; Li et al., 2015; Shangguan et al., 2013). Westermann et al. (2017) used geomorphological classification maps to parameterize large-scale patterns of ground thermal properties (e.g., sediment types, ground ice content, and surface properties) in the Siberian permafrost region. Similarly, in this study, we utilized an existing stratigraphic classification map, gridded to a 1 km^2 resolution, to account for the spatial-scale patterns of sediment types, ground ice, and surface properties in WKL, which were used to parameterize subsurface properties. The MVPM was calibrated using ground temperature measurements from boreholes, specific to each soil class and geographical location. This approach effectively captures large-scale differences, particularly in ALT (see Sect. 3.3.2). However, notable small-scale variability in ground properties is superimposed on these large-scale patterns, leading to significant variability in ALT and ground temperature that cannot be resolved at the 1 km scale. Furthermore, the stratigraphies assigned to each sediment class (Table 1) also may exhibit strong variability within each class, which can result in biased model outputs. Despite these limitations, we are confident that the key properties of the different sediment classes—critical for driving the dynamic response of ground temperatures to climate change—are accurately represented in our model. To further enhance the accuracy of permafrost thermal dynamics modeling, we emphasize~~

~~the importance of improving soil property datasets, particularly for permafrost regions.~~

Representation of soil stratigraphy: Accurate representation of soil properties is critical for modeling water and heat transport in frozen soils at both global and regional scales (Dai et al., 2019; Lawrence and Slater, 2008; Harp et al., 2016; Hu et al., 2023). However, most soil datasets used in models are based on data from seasonally frozen regions, and there remains a significant lack of coverage in the permafrost areas of the QTP, particularly for deeper soil layers (Hengl et al., 2017; Li et al., 2015; Shangguan et al., 2013). Westermann et al. (2017) addressed similar limitations in the Siberian permafrost region by using geomorphological classification maps to parameterize large-scale patterns of ground thermal properties such as sediment type, ground ice content, and surface characteristics.

In this study, we adopted a comparable approach by applying an existing stratigraphic classification map, gridded at 1 km² resolution to represent the spatial distribution of sediment types, ground ice, and surface properties in the WKL region. These classifications were then used to parameterize subsurface properties in our model. However, small-scale heterogeneity in ground conditions introduces considerable variability in ALT and ground temperature, which cannot be resolved at the 1-km resolution. Moreover, variability within each sediment class (Table 1) can result in biased model outputs.

To quantify model uncertainty, we conducted a one-at-a-time sensitivity analysis (Figure 12) using three representative boreholes located in stable permafrost, unstable permafrost, and seasonally frozen ground (see Table 4). Key model parameters were perturbed by ±10% to evaluate their effects on MAGT at 15 m depth and ALT. Among all parameters, upper boundary temperature (e.g., surface forcing) exerted the strongest influence on MAGT, though the absolute impact was modest, around ±0.5 °C in seasonally frozen ground and ≤±0.1 °C in permafrost areas. ALT showed similarly limited sensitivity, varying by ~±0.1 m in stable permafrost and ±0.05 m in unstable zones. Soil thermal conductivity and water/ice content had a more pronounced effect on ALT, particularly in unstable permafrost, where a 10% change could lead to a 0.05–0.1 m variation. In contrast, soil heat capacity had minimal influence on both MAGT and ALT.

These findings indicate that the model achieves thermal stability over the simulation period, and uncertainties related to stratigraphy exert limited impact on overall performance. Although stratigraphic classification and spatial variability introduce some unavoidable uncertainty, our approach is firmly grounded in field measurements and observed thermal properties. Despite these limitations, we are confident the model reliably captures the essential thermal characteristics of each sediment class, which are key to simulating permafrost dynamics. Continued improvements in subsurface datasets, particularly in permafrost regions, will be vital for refining future model performance.

Table 4. Information on three representative borehole sites used for one-at-a-time sensitivity analysis

Borehole	Description
ZK30	The borehole reaches a depth of 15 m, with the ground primarily composed of fine sand and silty sand. The MAGT is -1.66 °C, and the ALT is 2.4 m, classifying the site as stable permafrost.
ZK12	The borehole has a drilling depth of 13.5 m, with a vegetation-free surface. The core consists primarily of Fluvial sand and sand. Frozen soil was first encountered at a depth of 4.9 m, where small ice crystals are evenly distributed within a granular soil structure. Below 5.5 m, the frozen layer disappears, accompanied by a noticeable increase in ground temperature. The 4.9–5.5 m interval represents a transition zone, and the site is classified as unstable permafrost.
ZK13	No frozen soil was encountered during the drilling process, and the site is classified as seasonally frozen ground

Note: This information is compiled from Li et al. (2012) and Zhao et al. (2019).

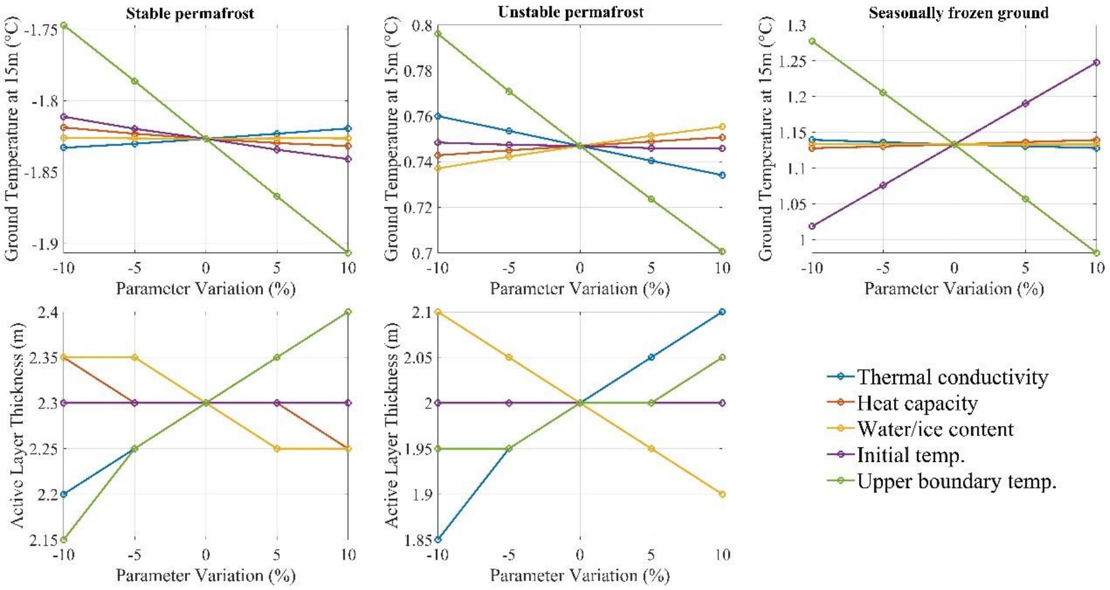

Figure 12. One-at-a-time sensitivity analysis showing the effects of ±10% variation in individual model parameters, e.g., soil thermal conductivity, heat capacity, water/ice content, initial temperature, and upper boundary temperature—on (top row) mean annual ground temperature (MAGT) at 15 m depth and (bottom row) active layer thickness (ALT), across

three ground conditions: stable permafrost (left), unstable permafrost (middle), and seasonally frozen ground (right).

6 Conclusions

The thermal state of permafrost is critically important for studying climate, ecology, hydrology, and engineering on the QTP. In this study, we quantitatively analyzed the spatiotemporal dynamics of the thermal regime across diverse environmental settings in a remote region (e.g., WKL) of the northwestern QTP ~~Tibetan Plateau~~ from 1980-2020. This is based on an enhanced numerical model, MVPM. We employed clustering approaches and parallel computing techniques to enhance computational efficiency. The model forcing data, remote-sensing-based land surface temperature dating back to 1980, with a spatial resolution of 1 km×1 km and a temporal resolution of 1 month, was constructed by using machine learning techniques to integrate field observations, satellite data and reanalysis products. Soil properties were parameterized using a geomorphological classification map, supplemented by in situ measurements of ground temperature and ALT. The key conclusions drawn from this study are summarized below:

- Compared to traditional atmospheric forcing, new reconstructed model forcing enables simulations of the permafrost thermal state with a much higher degree of precisions and spatial resolution than traditional methods. The thermal state of permafrost was reproduced within a range of ±0.25°C at 10 m, and ALT was reproduced within ±0.25 m.

- The 80% permafrost thermal regime in WKL is relatively stable, with initial MAGT15m ranging from −7.5°C to −1.5°C. Spatially, the highest MAGT15m around −0.5°C, and the deepest ALT, ranging from 2.5m to 3.0m, were modeled in low-elevation areas below 4,800m a.s.l. In contrast, the lowest ground temperatures, dropping below −10°C, and the shallowest ALT, less than 1 m, were modeled in high-elevation regions above 5,600m a.s.l. Additionally, the alluvial plain sedimentary class exhibited the deepest ALT, with an average of 2.5m, while the glarosion sedimentary class had the shallowest ALT, averaging 1.5 m.

- From 1980 to 2022, the WKL permafrost survey area experienced a significant warming trend in LST, with an average increase of 0.40°C per decade. In response to this warming, 58.58% of the area exhibited a warming trend in MAGT15m. The most pronounced warming, averaging 0.3°C, was simulated in high-elevation areas above 5,600 m a.s.l., characterized by stable permafrost. Changes in ALT were closely linked to regional climate fluctuations and soil stratigraphic classifications. The greatest deepening of the ALT was modeled in alluvial and lacustrine sediment classes, with an increase exceeding 0.17 m. In contrast, the smallest change, an increase of 0.11 m, was observed in the glarosion sediment class. Meanwhile, the spatial distribution of permafrost in the WKL remained relatively stable during this period, with less than 0.5%~~ experiencing recover or degradation~~ experiencing recovery or degradation.

Code and data availability

In situ monitoring data from the field observation sites provided by the Cryosphere Research Station on Qinghai–Xizang Plateau of the Chinese Academy of Sciences (CAS) are available online at National Tibetan Plateau Data Center (TPDC): https://data.tpdc.ac.cn/en/ disallow/789e838e-16ac-4539-bb7e-906217305a1d/, December 12, 2024 (Zhao et al.,2021); Zhao et al. (2019b) (Permafrost and environment changes on the Qinghai-Tibetan Plateau. Beijing, China: Science Press); ~~-~~Li et al. (2012) (Permafrost distribution in typical area of west Kunlun Mountains derived from a comprehensive survey (in Chines with English abstract), J. GLACIOL.).

Enhanced MODIS LST data since 2003 were ~~provided~~ obtained by Zou et al. (2017) (https://doi.org/10.5194/tc-11-2527-2017).

Daily Air temperature and precipitation from 1961-2019 were provided by Qin et al. (2022) (https://doi.pangaea.de/10.1594/PANGAEA.941329, December 12, 2024).

CN05.1 datasets available on request from: wangjun@mail.iap.ac.cn (https://ccrc.iap.ac.cn/resource/detail?id=228, December 12, 2024).

Additional datasets used in this study include:

Skin temperature dataset was download from ECMFW https://cds.climate.copernicus.eu/datasets/reanalysis-era5-land?tab=overview, December 12, 2024).

Soil temperature dataset was download from NCEP Climate Forecast System Reanalysis (CFSR, https://rda.ucar.edu/datasets/ds093.0/dataaccess/ December 12, 2024).

Fractional cloud cover and surface radiation budget dataset was download from EUMETSAT, CM SAF (https://wui.cmsaf.eu/safira/action/viewDoiDetails?acronym=CLARA_AVHRR_V003, December 12, 2024).

Leaf area index (LAI) dataset is from Global Land Surface Satellite (GLASS) and MODIS (Global LAnd Surface Satellite (GLASS); https://modis.gsfc.nasa.gov/data/dataprod/mod15.php;

December 12, 2024).

Topography:~~he~~ Shuttle Radar Topography Mission (SRTM) with a 1 arcsec (~30 m) DEM data were from Hole-filled seamless SRTM data V4, International Center for Tropical Agriculture (CIAT), available at http: //srtm.csi.cgiar.org (Jarvis et al., 2008).

Background maps of China: ~~The background maps of China are provided by~~ Wen et al. (2024, https://doi.org/10.1007/s10584-024-03712-7). T

Tibetan Plateau boundary: Zhang (2019a), available from National Tibetan Plateau Data Center (TPDC) (http://data.tpdc.ac.cn/zh-hans/, December 12, 2024).

Geological sediment classification and lakes: Zhou et al. (2007); Zhang et al. (2019b), available from TPDC: http://data.tpdc.ac.cn/zh-hans/ (accessed December 12, 2024).

~~he Tibet Plateau boundary (Zhang, 2019a) and the geological sediment classification map (Zhou et al., 2007), along with the lake dataset (Zhang et al., 2019b) is freely available from the National Tibetan Plateau Data Center (http://data.tpdc.ac.cn/zh-hans/, December 12, 2024).~~

The glacier inventory: ~~comes from the~~ Second Glacier Inventory Dataset of China (Guo et al., 2015, doi: 10.3189/2015JoG14J209).

Four existing permafrost distribution maps: Li et al. (1996) ,~~Gansu Culture Press, Lanzhou) and~~ Wang et al. (2006)~~ (Chinese Map Press, Beijing, China),~~ and Zou et al. (2017) ~~(https://doi.org/10.5194/tc-11-2527-2017) can free download from National Tibetan Plateau Data Center (http://data.tpdc.ac.cn/zh-hans/, December 12, 2024);=~~ Cao et al. 2023 ~~(https://doi.org/10.5194/essd-15-3905-2023, December 12, 2024).~~, all available via TPDC.

~~The new permafrost model source code is available on request from the following co-authors of this study: Jianting Zhao (first author), jt.zhao@nuist.edu.cn; Lin Zhao (corresponding author), lzhao@nuist.edu.cn; and Zhe Sun, sunzhe@lzb.ac.cn.~~

Model code availability

The permafrost model source code developed for this study is available upon request from the following co-authors: Jianting Zhao (first author): jt.zhao@nuist.edu.cn; Lin Zhao (corresponding author): lzhao@nuist.edu.cn; Zhe Sun: sunzhe@lzb.ac.cn

Author contributions

LZ conceived and conceptualized the idea; JZ and ZS developed the methodology; LZ, ZS, GH, and WZ supervised the study; JZ performed data processing and analyses. LZ, ZS and GH acquired the funding and provided the resources; DZ, GL, QP, ED, ZL, XW, and YX participated in the fieldwork and maintained the observation sites; JZ wrote the manuscript, and LZ, ZS, GH, MX, LW, and WZ reviewed and edited the writing.

Declaring of competing interest

The contact author has declared that none of the authors has any competing interests.

Acknowledgments

Warm thanks to all the scientists, engineers, and students who participated in the field investigations and measurements, and helped maintain the observation network for data collection ~~acquisition.~~

Financial support

Financial support for this research was provided by the National Natural Science Foundation of China (grant no.41931180, 42322608, and 42401149); the Second Tibetan Plateau Scientific Expedition and Research (STEP) Program, China (grant no. 2019QZKK0201); China Postdoctoral Science Foundation funded project (grant no.2022M721670); Guangxi Natural Science Foundation (grant no. 2024GXNSFBA010295) and China Scholarship Council (grant no. 202309040044).

References

Allen, D. M., Michel, F. A., and Judge, A. S.: The permafrost regime in the Mackenzie Delta, Beaufort Sea region, N.W.T. and its significance to the reconstruction of the paleoclimatic history, J. Quaternary Sci., 3, 3–13, https://doi.org/10.1002/jqs.3390030103, 1988.

Baldwin, J., and Vecchi, G.: Influence of the Tian Shan on arid extratropical Asia, J. Clim., 29(16), 5741-5762, https://doi.org/10.1175/JCLI-D-15-0490.1, 2016.

Barber, V. A., Juday, G. P., Finney, B. P., and Wilmking, M.: Reconstruction of Summer Temperatures in Interior Alaska from Tree-Ring Proxies: Evidence for Changing Synoptic Climate Regimes, Clim. Change, 63, 91–120, https://doi.org/10.1023/B:CLIM.0000018501.98266.55, 2004.

Bense, V. F., Kooi, H., Ferguson, G., and Read, T.: Permafrost degradation as a control on hydrogeological regime shifts in a warming climate, J. GEOPHYS. RES-EARTH,117(F3), https://doi.org/10.1029/2011JF002143, 2012.

Boike, J., Georgi, C., Kirilin, G., Muster, S., Abramova, K., Fedorova, I., Chetverova, A., Grigoriev, M., Bornemann, N., and Langer, M.: Thermal processes of thermokarst lakes in the continuous permafrost zone of northern Siberia–observations and modeling (Lena River Delta, Siberia), Biogeosciences, 12, 5941–5965, https://doi.org/10.5194/bg-12-5941-2015, 2015.

Breiman, L.: Random forests. Machine learning,45, 5-32, 2001.

Burke, E. J., Zhang, Y., and Krinner, G.: Evaluating permafrost physics in the Coupled Model Intercomparison Project 6 (CMIP6) models and their sensitivity to climate change, The Cryosphere, 14, 3155–3174, https://doi.org/10.5194/tc-14-3155-2020, 2020.

Cable, W. L., Romanovsky, V. E., and Jorgenson, M. T.: Scaling-up permafrost thermal measurements in western Alaska using an ecotype approach, The Cryosphere, 10, 2517–2532, https://doi.org/10.5194/tc-10-2517-2016, 2016.

Cannon, F., Carvalho, L. M. V., Jones, C., and Norris, J.: Winter westerly disturbance dynamics and precipitation in the Western Himalaya and Karakoram: A wave-tracking approach, Theor. Appl. Climatol.,125(1–2),27–44, https://doi.org/10.1007/s00704-015-1489-8, 2016.

Cao, B., Zhang, T., Wu, Q., Sheng, Y., Zhao, L., and Zou, D.: Brief communication: Evaluation and inter-comparisons of Qinghai–Tibet Plateau permafrost maps based on a new inventory of field evidence, The Cryosphere, 13, 511–519, https://doi.org/10.5194/tc-13-511-2019, 2019.

Cao, Z., Nan, Z., Hu, J., Chen, Y., and Zhang, Y.: A new 2010 permafrost distribution map over the Qinghai–Tibet Plateau based on subregion survey maps: a benchmark for regional permafrost modeling, Earth Syst. Sci. Data, 15, 3905–3930, https://doi.org/10.5194/essd-15-3905-2023, 2023.

Chen, H., Nan, Z., Zhao, L., Ding, Y., Chen, J., and Pang, Q.: Noah modelling of the permafrost distribution and characteristics in the West Kunlun area, Qinghai-Tibet Plateau, China, Permafrost and Periglac. Process., 26(2), 160-174, https://doi.org/10.1002/ppp.1841, 2015

Cheng, G., Zhao, L., Li, R., Wu, X., Sheng, Y., Hu, G., Zou, D., Jin, H., Li, X., and Wu, Q.: Characteristic, changes and impacts of permafrost on Qinghai-Tibet plateau (in Chinese with

English abstract), Chin Sci Bull., 64(27):2783-2795, doi: 10.1360/TB-2019-0191, 2019.

Dai, Y., Shangguan, W., Wei, N., Xin, Q., Yuan, H., Zhang, S., Liu, S., Lu, X., Wang, D., and Yan, F.: A review of the global soil property maps for Earth system models, SOIL, 5, 137–158, https://doi.org/10.5194/soil-5-137-2019, 2019.

Fiddes, J., Endrizzi, S., and Gruber, S.: Large-area land surface simulations in heterogeneous terrain driven by global data sets: application to mountain permafrost, The Cryosphere, 9, 411–426, https://doi.org/10.5194/tc-9-411-2015, 2015.

Guo, D. and Wang, H.: CMIP5 permafrost degradation projection: a comparison among different regions. J. Geophys. Res.-Atmos.,121, 4499–4517, https://doi.org/10.1002/2015JD024108, 2016.

Guo, D., Wang, H., and Li, D.: A projection of permafrost degradation on the Tibetan Plateau during the 21st century, 117, D05106, J. Geophys. Res.-Atmos., 117, D05106, https://doi.org/10.1029/2011JD016545, 2012.

Guo, D., Wang, H., and Wang, A.: Sensitivity of historical simulation of the permafrost to different atmospheric forcing data sets from 1979 to 2009, J. Geophys. Res.,122(22), 12-269, https://doi.org/10.1002/2017JD027477,2017.

Harp, D. R., Atchley, A. L., Painter, S. L., Coon, E. T., Wilson, C. J., Romanovsky, V. E., and Rowland, J. C.: Effect of soil property uncertainties on permafrost thaw projections: a calibration-constrained analysis, The Cryosphere, 10, 341–358, https://doi.org/10.5194/tc-10-341-2016, 2016.

Harrison, W. D.: Permafrost response to surface temperature change and its implications for the 40,000-year surface temperature history at Prudhoe Bay, Alaska, J. Geophys. Res.-Sol. Ea., 96, 683– 695, https://doi.org/10.1029/90JB02004, 1991

Hengl, T., Mendes de Jesus, J., Heuvelink, G. B., Ruiperez Gonzalez, M., Kilibarda, M., Blagotić, Shangguan, W., Wright, M. N., Geng, X., Marschallinger, B.B., Guevara, M., Vargas, R., MacMillan, R.A., Batjes, N. H., Leenaars, J. Ribeiro, E., Wheeler, I., Mantel, S., and Kempen, B.: SoilGrids250m: Global gridded soil information based on machine learning, PLoS. one, 12(2), e0169748, https://doi.org/10.1371/journal.pone.0169748, 2017.

Hjort, J., Streletskiy, D., Doré, G.,Wu, Q., Bjella, K., and Luoto, M.: Impacts of permafrost degradation on infrastructure. Nat. Rev. Earth Environ.,3, 24–38, https://doi.org/10.1038/s43017-021-00247-8, 2022.

Hu, G., Zhao, L., Li, R., Park, H., Wu, X., Su, Y., Guggenberger, G., Wu, T., Zou, D., Zhu, X., Zhang, W., Wu, Y., and Hao, J: Water and heat coupling processes and its simulation in frozen soils: Current status and future research directions, Catena, 222, 106844, https://doi.org/10.1016/j.catena.2022.106844, 2023.

Hu, G., Zhao, L., Li, R., Wu, X., Wu, T., Xie, C., Zhu, X., and Su, Y.: Variations in soil temperature from 1980 to 2015 in permafrost regions on the Qinghai-Tibetan Plateau based on observed and reanalysis products, Geoderma, 337, 893-905, https://doi.org/10.1016/j.geoderma.2018.10.044, 2019.

Hu, J., Zhao, L., Wang, C., Hu, G., Zou, D., Xing, Z., Jiao, M., Qiao, Y., Liu, G., and Du, E.: Applicability evaluation and correction of CLDAS surface temperature products in permafrost region of Qinghai-Tibet Plateau (in Chinese with English abstract), Climate Change Research, 20 (1): 10-25, DOI: 10.12006/j.issn.1673-1719.2023.033, 2024

Hu, S., He, L., and Wang, J.: Heat flow in the continental area of China: a new data set. Earth and Planetary Science Letters,179(2), 407-419, https://doi.org/10.1016/S0012-821X(00)00126-6, 2000.

Hu, Y., Liu, L., Huang, L., Zhao, L., Wu, T., Wang, X., and Cai, J.: Mapping and characterizing rock glaciers in the arid Western Kunlun Mountains supported by InSAR and deep learning, J. GEOPHYS. RES-EARTH,128(9), e2023JF007206, https://doi.org/10.1029/2023JF007206, 2023.

IPCC. Climate change 2021: the physical science basis, https://www.ipcc.ch/report/ar6/wg1/downloads/report/IPCC_AR6_WGI_Full_Report.pdf., 2021.

IPCC.: Special report on the ocean and cryosphere in a changing climate, https://archive.ipcc.ch/srocc/, 2019.

Jafarov, E. E., Marchenko, S. S., and Romanovsky, V. E.: Numerical modeling of permafrost dynamics in Alaska using a high spatial resolution dataset, The Cryosphere, 6, 613–624, https://doi.org/10.5194/tc-6-613-2012, 2012

Jiao, M., Zhao, L., Wang, C., Hu, G., Li, Y., Zhao, J., Zou, D., Xing, Z., Qiao, Y., Liu, G., Du, E., Xiao, M., and Hou, Y.: Spatiotemporal variations of soil temperature at 10 and 50 cm depths in permafrost regions along the Qinghai-Tibet engineering corridor, Remote Sens. 2023, 15(2), 455; https://doi.org/10.3390/rs15020455, 2023.

Jin, H., Yu, Q., Wang, S., and Lü, L.: Changes in permafrost environments along the Qinghai–Tibet engineering corridor induced by anthropogenic activities and climate warming, Cold Reg. Sci. Technol.,53, 317-333, https://doi.org/10.1016/j.coldregions.2007.07.005, 2008.

Jin, H., Luo, D., Wang, S., Lü, L., and Wu, J.: Spatiotemporal variability of permafrost degradation on the Qinghai-Tibet Plateau, Sci. Cold Arid Reg., 3, 281–305, DOI: 10.3724/SP.J.1226.2011.00281, 2011.

Jin, H., Wu, Q., and Romanovsky, V.: E. Degrading permafrost and its impacts, Adv. Clim. Chang. Res., 12(1), 1-5, https://doi.org/10.1016/j.accre.2021.01.007, 2021.

Kneier, F., Overduin, P. P., Langer, M., Boike, J., and Grigoriev, M. N.: Borehole temperature reconstructions reveal differences in past surface temperature trends for the permafrost in the Laptev Sea region, Russian Arctic, arktos, 4, 1–17, 2018.

Koven, C., William J., and Alex S.: Analysis of Permafrost Thermal Dynamics and Response to Climate Change in the CMIP5 Earth System Models, J. Clim., 26,1877-1900, https://doi.org/10.1175/JCLI-D-12-00228.1, 2013.

Kurylyk, B. L., Hayashi, M., Quinton, W. L., McKenzie, J. M., and Voss, C. I. Influence of vertical and lateral heat transfer on permafrost thaw, peatland landscape transition, and groundwater flow, Water Resour. Res., 52(2), 1286-1305, https://doi.org/10.1002/2015WR018057, 2016.

Lachenbruch, A. H. and Marshall, B. V.: Changing Climate: Geothermal Evidence from Permafrost in the Alaskan Arctic, Science, 234, 689–696, https://doi.org/10.1126/science.234.4777.689, 1986.

Lafrenière, M., and Lamoureux, S.: Effects of changing permafrost conditions on hydrological processes and fluvial fluxes, Earth-Sci. Rev., 191, 212-223, https://doi.org/10.1016/j.earscirev.2019.02.018, 2019.

Langer, M., Nitzbon, J., Groenke, B., Assmann, L.-M., Schneider von Deimling, T., Stuenzi, S. M., and Westermann, S.: The evolution of Arctic permafrost over the last 3 centuries from ensemble simulations with the CryoGridLite permafrost model, The Cryosphere, 18, 363–385, https://doi.org/10.5194/tc-18-363-2024, 2024.

Langer, M., Westermann, S., Heikenfeld, M., Dorn, W., and Boike, J.: Satellite-based modeling of permafrost temperatures in a tundra lowland landscape, Remote Sens. Environ.,135, 12-24, https://doi.org/10.1016/j.rse.2013.03.011, 2013.

Lawrence, D.M., Slater, A.G., and Swenson, S.C., Simulation of Present-Day and Future Permafrost and Seasonally Frozen Ground Conditions in CCSM4, J. Clim., 25, 2207–2225, https://doi.org/10.1175/JCLI-D-11-00334.1, 2012.

Lawrence, D.M., Slater, A.G., Romanovsky, V.E., and Nicolsky, D.J.: Sensitivity of a model projection of near-surface permafrost degradation to soil column depth and representation of soil organic matter, J. Geophys. Res.-Earth Surface, 113 (F2), https://doi.org/10.1029/2007JF000883, 2008.

Li, K., Chen, J., Zhao, L., Zhang, X., Pang, Q., Fang, H., Liu, G.: Permafrost distribution in typical area of west Kunlun Mountains derived from a comprehensive survey (in Chines with English abstract), J. GLACIOL.,2012.

Li, N., Cuo, L., Zhang, Y., and Ding, J.: The synthesis of potential factors contributing to the asynchronous warming between air and shallow ground since the 2000s on the Tibetan Plateau, Geoderma,441, 116753, https://doi.org/10.1016/j.geoderma.2023.116753, 2024.

Li, R., Zhao, L., Ding, Y., Wu, T., Xiao, Y., Du, E., Liu, G., and Qiao, Y.: Temporal and spatial variations of the active layer along the Qinghai-Tibet Highway in a permafrost region, Chinese Sci. Bull., 57, 4609–4616, https://doi.org/10.1007/s11434-012-5323- 8, 2012.

Li, S., and Li, S.: Significance and research on the two boreholes of Tianshuihai in the west Kunlun Mountains (in Chinese with English abstract), J. GLACIOL., (13) 2,1991.

Li, S. and Cheng, G.: Map of Frozen Ground on Qinghai-Xizang Plateau, Gansu Culture Press, Lanzhou, 1996

Li, W., Zhao, L., Wu, X., Wang, S., Nan, Z., Fang, H., and Shi, W.: Distribution of Soils and Landform Relationships in Permafrost Regions of the Western Qinghai-Xizang (Tibetan) Plateau, China, Soil. Sci., 179, 348–357, doi: 10.1097/SS.0000000000000075, 2014.

Li, W., Zhao, L., Wu, X., Zhao, Y., Fang, H., and Shi, W.: Distribution of soils and landform relationships in the permafrost regions of Qinghai-Xizang (Tibetan) Plateau, Chinese Sci. Bull., 60, 2216–2226, https://doi.org/10.1360/N972014-01206, 2015.

Liu, G., Xie, C., Zhao, L., Xiao, Y., Wu, T., Wang, W., and Liu, W.: Permafrost warming near the northern limit of permafrost on the Qinghai–Tibetan Plateau during the period from 2005 to 2017, A case study in the Xidatan area, Permafrost Periglac.,32, 323–334, https://doi.org/10.1002/ppp.2089, 2020.

Marchenko, S.S., Bjella, K., Nicolsky, D. J., Romanovsky, V. E.: Modeling Dynamics of Permafrost Degradation and their Impact on Ecosystems Across Entire Alaska: Arctic and Subarctic Engineering Design Tool (Part-1). Preprints, 2024030927. https://doi.org/10.20944/preprints202403.0927.v2, 2024.

Miner, K., D'Andrilli, J., Mackelprang, R., Edwards, A., Malaska, M., Waldrop, M., and Miller, C.: Emergent biogeochemical risks from Arctic permafrost degradation. Nat. Clim. Chang.11, 809–819. https://doi.org/10.1038/s41558-021-01162-y, 2021.

Ni, J., Wu, T., Zhu, X., Hu, G., Zou, D., Wu, X., Li, R., Xie, C., Qiao, Y., Pang, Q., Hao, J., and Yang, C.: Simulation of the present and future projection of permafrost on the Qinghai-Tibet Plateau with statistical and machine learning models, J. Geophys. Res. Atmos, 126(2), e2020JD033402, https://doi.org/10.1029/2020JD033402, 2021

Nicolsky, D. J., Romanovsky, V. E., and Tipenko, G. S.: Using in-situ temperature measurements to estimate saturated soil thermal properties by solving a sequence of optimization problems, The Cryosphere, 1, 41–58, https://doi.org/10.5194/tc-1-41-2007, 2007.

Nicolsky, D. J., Romanovsky, V. E., Panda, S. K., Marchenko, S. S., and Muskett, R. R.: Applicability of the ecosystem type approach to model permafrost dynamics across the Alaska North Slope. J. GEOPHYS. RES-EARTH, 122(1), 50-75, https://doi.org/10.1002/2016JF003852, 2017.

Noetzli, J. and Gruber, S.: Transient thermal effects in Alpine permafrost, The Cryosphere, 3, 85–99, https://doi.org/10.5194/tc-3-85-2009, 2009

O'Neill, H., Burn, C., Allard, M., Arenson, L., Bunn, M., Connon, R., Kokelj, S., Kokelj, S., LeBlanc, A., Morse, P., and Smith, S.: Permafrost thaw and northern development, Nat. Clim.

Chang.,10, 722–723, https://doi.org/10.1038/s41558-020-0862-5, 2020.

Osterkamp, T. E. and Gosink, J. P.: Variations in permafrost thickness in response to changes in paleoclimate, J. Geophys. Res.- Sol. Ea., 96, 4423–4434, https://doi.org/10.1029/90JB02492, 1991.

Qin, R., Zhao, Z., Xu, J., Ye, J.-S., Li, F.-M., and Zhang, F.: HRLT: a high-resolution (1 d, 1 km) and long-term (1961–2019) gridded dataset for surface temperature and precipitation across China, Earth Syst. Sci. Data, 14, 4793–4810, https://doi.org/10.5194/essd-14-4793-2022, 2022

Qin, Y., Liu, W., Guo, Z., and Xue, S.: Spatial and temporal variations in soil temperatures over the Qinghai Tibet Plateau from 1980 to 2017 based on reanalysis products, Theor. Appl. Climatol. 140 (3e4), 1055e1069. https://doi.org/10.1007/s00704-020-03149-9, 2020.

Schiesser, W.: The Numerical Method of Lines: Integration of Partial Differential Equations, vol. 212, Academic Press, San Diego, USA, 1991.

Schoeneich,P., Romanovsky, V., Lewkowicz, A., Abramov, A., Allard1, M., Boike, J., Cable, W., Christiansen, H., Delaloye, R., Diekmann, B., Drozdov, D., Etzelmüller, B., Guido Grosse, G., Guglielmin, M., Ingeman-Nielsen, T., Ketil Isaksen, K., Ishikawa, M., Margareta Johansson, M., Johannsson, H., Joo, A., Kaverin, D., Kholodov, A., Konstantinov, P., Kröger, T., Christophe Lambiel, C., Jean-Pierre Lanckman, J., Luo, D., Galina Malkova, G., Meiklejohn, I., Natalia Moskalenko, N., Oliva, M., Phillips, M., Ramos, M., Sannel, A., Dmitrii Sergeev, D., Seybold, C., Skryabin, P., Vasiliev, A., Wu, Q., Yoshikawa, K., Mikhail Zheleznyak, M., and Lantuit, H.: Permafrost is warming at a global scale, Nat. Commun.,10, 264, https://doi.org/10.1038/s41467-018-08240-4, 2019.

Schuur, E., McGuire, A., Schadel1, C., Grosse, G., Harden, J., Hayes, D., Hugelius, G.,Koven, C., Kuhry, P., Lawrence, D., Natali, S., Olefeldt, D., Romanovsky, V., Schaefer, K., Turetsky, M., Treat, C., and & Vonk, J.: Climate change and the permafrost carbon feedback, Nature, 520, 171–179, https://doi.org/10.1038/nature14338, 2015.

Shangguan, W., Dai, Y., Liu, B., Zhu., A., Duan, Q., Wu, L., Ji, D., Ye, A., Yuan, H., Zhang, Q., Chen, D., Chen, M., Chu, J., Dou, Y., Guo, J., Li, H., Li, J., Liang, L., Liang, X., Liu, H., Liu, S., Miao, C., and Zhang, Y.: A China data set of soil properties for land surface modeling, J. Adv. Model. Earth Syst.,5,212–224, https://doi.org/10.1002/jame.20026, 2013.

Sheng, Y., Ma, S., Cao, W., and Wu, J.: Spatiotemporal changes of permafrost in the Headwater Area of the Yellow River under a changing climate, Land Degrad. De.,31(1), 133-152, https://doi.org/10.1002/ldr.3434, 2020.

Sjöberg, Y., Coon, E., Sannel, A., Pannetier, R., Harp, D., Frampton, A., Painter, S., Lyon SW.: Thermal effects of groundwater flow through subarctic fens: a case study based on field observations and numerical modeling, Water Resour. Res., 52:1591–1606.https://doi.org/10.1002/2015WR017571, 2016.

Slater, A.G., and Lawrence, D.M.: Diagnosing present and future permafrost from climate models, J. Clim. 26 (15), 5608e5623, https://doi.org/ 10.1175/jcli-d-12-00341.1, 2013

Smith, S., O'Neill, H., Isaksen, K., Noetzli, J., and Romanovsky, V.: The changing thermal state of permafrost, Nat. Rev. Earth Environ., 3, 10–23, https://doi.org/10.1038/s43017-021-00240-1, 2022.

Su, B., Huang, J., Gemmer, M., Jian, D., Tao, H., Jiang, T., and Zhao, C.: Statistical downscaling of CMIP5 multi-model ensemble for projected changes of climate in the Indus River Basin, Atmos. Res, 178, 138-149, https://doi.org/10.1016/j.atmosres.2016.03.023 ,2016.

Sun, Z., Zhao, L., Hu, G., Qiao, Y., Du, E., Zou, D., Xie, C.: Modeling permafrost changes on the Qinghai-Tibetan plateau from 1966 to 2100: a case study from two boreholes along the Qinghai-Tibet engineering corridor, Permafrost and Periglac. Process., 32:156-171, https://doi.org/10.1002/ppp.2022, 2019.

Sun, Z., Zhao, L., Hu, G., Zhou, H., Liu, S., Qiao, Y., Du, E., Zou, D., and Xie, C.: Numerical simulation of thaw settlement and permafrost changes at three sites along the Qinghai-Tibet Engineering Corridor in a warming climate, Geophys. Res. Lett., 49, e2021GL097334, https://doi.org/10.1029/2021GL097334, 2022.

Sun, Z., Zhao, L., Hu, G., Zhou, H., Liu, S., Qiao, Y., Du, E., Zou, D., and Xie, C.: Effects of Ground Subsidence on Permafrost Simulation Related to Climate Warming, Atmosphere,15(1), 12, https://doi.org/ 10.3390/atmos15010012, 2023.

Walvoord, M., and Kurylyk, B.; Hydrologic Impacts of Thawing Permafrost—A Review. Vadose Zone Journal,15 (6): vzj2016.01.0010, doi: https://doi.org/10.2136/vzj2016.01.0010, 2016.

Wang, L., Zhao, L., Zhou, H., Liu, S., Hu, G., Li, Z., Wang, C., and Zhao, J.: Evidence of ground ice melting detected by InSAR and in situ monitoring over permafrost terrain on the Qinghai-Xizang (Tibet) Plateau, Permafrost and Periglac. Process., 34(1): 52-67. doi:10.1002/ppp.2171, 2023.

Wang, S., Sheng, Y., Li, J., Wu, J., Cao, W., and Ma, S.: An estimation of ground ice volumes in permafrost layers in Northeastern Qinghai-Tibet Plateau, China. Chin. Geogra. Sci.,28, 61-73, https://doi.org/10.1007/s11769-018-0932-z, 2018.

Wang, T., Wang, N., and Li, S.: Map of the glaciers, frozen ground and desert in China, 1: 4 000 000, Chinese Map Press, Beijing, China, 2006.

Wang, Z., Wang, Q., Zhao, L., Wu, X., Yue, G., Zou, D., Nan, Z., Liu, G., Pang, Q., Fang, H., Wu, T., Shi, J., Jiao, K., Zhao, Y., and Zhang, L.: Mapping the vegetation distribution of the permafrost zone on the Qinghai-Tibet Plateau, J. Mt. Sci., 13, 1035–1046, http://jms.imde.ac.cn, 2016.

Wen, S., Su, B., Huang, J., Wang, Y., Treu, S., Jiang, F., Jiang, S., and Jiang, H.: Attribution of streamflow changes during 1961–2019 in the Upper Yangtze and the Upper Yellow River basins, Clim. Change, 177(4), 60, https://doi.org/10.1007/s10584-024-03712-7, 2024

Westermann, S., Østby, T. I., Gisnås, K., Schuler, T. V., and Etzelmüller, B.: A ground temperature map of the North Atlantic permafrost region based on remote sensing and reanalysis data, The Cryosphere, 9, 1303–1319, https://doi.org/10.5194/tc-9-1303-2015, 2015.

Westermann, S., Peter, M., Langer, M., Schwamborn, G., Schirrmeister, L., Etzelmüller, B., and Boike, J.: Transient modeling of the ground thermal conditions using satellite data in the Lena River delta, Siberia, The Cryosphere, 11, 1441–1463, https://doi.org/10.5194/tc-11-1441-2017, 2017.

Westermann, S., Schuler, T. V., Gisnås, K., and Etzelmüller, B.: Transient thermal modeling of permafrost conditions in Southern Norway, The Cryosphere, 7, 719–739, https://doi.org/10.5194/tc-7-719-2013, 2013.

Wu, J., and Gao, X.: A gridded daily observation dataset over China region and comparison with the other datasets (in Chinese with English abstract), Chinese J. Geophys., 56(04):1102-1111, dio:10.6038/cjg20120406, 2013.

Wu, J., Sheng, Y., Wu, Q., and Wen, Z.: Processes and modes of permafrost degradation on the

Qinghai-Tibet Plateau, Sci. China Ser. D-Earth Sci., 53,150–158, https://doi.org/10.1007/s11430-009-0198-5,2010.

Wu, X., Nan, Z., Zhao, S., Zhao, L., and Cheng, G.: Spatial modeling of permafrost distribution and properties on the Qinghai-Tibet Plateau, Permafrost and Periglac. Process., 29, 86-99, https://doi.org/10.1002/ppp.1971, 2018.

Xiao, Y., Zhao, L., Dai, Y., Li, R., Pang, Q., and Yao, J.: Representing permafrost properties in CoLM for the Qinghai–Xizang (Tibetan) plateau, Cold Reg. Sci. Technol., 87, 68-77, http://dx.doi.org/10.1016/j.coldregions.2012.12.004, 2013.

Xing, Z., Zhao, L., Fan, L., Hu, G., Zou, D., Wang, C., Liu, S., Du, E., Xiao, Y., Li, R., Liu, G., Qiao, Y., and Shi, J.: Changes in the ground surface temperature in permafrost regions along the Qinghai–Tibet engineering corridor from 1900 to 2014: a modified assessment of CMIP6, Adv. Clim. Chang. Res.,14(1), 85-96, https://doi.org/10.1016/j.accre.2023.01.007, 2023.

Yang, S., Li, R., Wu, T., Hu, G., Xiao, Y., Du, Y., Zhu, X., Ni, J., Ma, J., Zhang, Y., and Shi, J.: Evaluation of reanalysis soil temperature and soil moisture products in permafrost regions on the Qinghai Tibetan Plateau, Geoderma,377 (1), 114583. https://doi.org/10.1016/j.geoderma. 2020.114583, 2020.

Yao, T., Xue, Y., Chen, D., Chen, F., Thompson, L., Cui, P., Koike, T., Lau, W. K., Lettenmaier, D., Mosbrugger, V., Zhang, R., Xu, B., Dozier, J., Gillespie, T., Gu, Y., Kang, S., Piao, S., Sugimoto, S., Ueno, K., Wang, L., Wang, W., Zhang, F., Sheng, Y., Guo, W., , Yang, X., Ma, Y., Shen, S. S. P., Su, Z., Chen, F., Liang, S., Liu, Y., Singh, V. P., Yang, K., Yang, D., Zhao, X., Qian, Y., Zhang, Y., and Li, Q.: Recent Third Pole's Rapid Warming Accompanies Cryospheric Melt and Water Cycle Intensification and Interactions between Monsoon and Environment: Multidisciplinary Approach with Observations, Modeling, and Analysis, B. Am. Meteorol. Soc., 100, 423-444, https://doi.org/10.1175/BAMS-D-17-0057.1, 2019.

Yi, Y., Kimball, J. S., Chen, R. H., Moghaddam, M., Reichle, R. H., Mishra, U., Zona, D., and Oechel, W. C.: Characterizing permafrost active layer dynamics and sensitivity to landscape spatial heterogeneity in Alaska, The Cryosphere, 12, 145–161, https://doi.org/10.5194/tc-12-145-2018, 2018.

You, Q., Cai, Z., Pepin, N., Chen, D., Ahrens, B., Jiang, Z., Wu, F., Kang, S., Zhang, R., Wu, T., Wang, P., Li, M., Zou, Z., Gao, Y., Zhai, P., and Zhang, Y.: Warming amplification over the

Arctic Pole and Third Pole: Trends, mechanisms and consequences. Earth Sci. Rev.,217, 103625, https://doi.org/10.1016/j.earscirev.2021.103625, 2021.

Zhang, Y., Olthof, I., Fraser, R., and Wolfe, S. A.: A new approach to mapping permafrost and change incorporating uncertainties in ground conditions and climate projections, The Cryosphere, 8, 2177–2194, https://doi.org/10.5194/tc-8-2177-2014, 2014.

Zhang, Y., Wang, X., Fraser, R., Olthof, I., Chen, W., Mclennan, D., Ponomarenko, S., and Wu, W.: Modelling and mapping climate change impacts on permafrost at high spatial resolution for an Arctic region with complex terrain, The Cryosphere, 7, 1121–1137, https://doi.org/10.5194/tc-7-1121-2013, 2013.

Zhao, J., Zhao, L., Sun, Z., Niu, F., Hu, G., Zou, D., Liu, G., Du, E., Wang, C., Wang, L., Qiao, Y., Shi, J., Zhang, Y., Gao, J., Wang, Y., Li, Y., Yu, W., Zhou, H., Xing, Z., Xiao, M., Yin, L., and Wang, S.: Simulating the current and future northern limit of permafrost on the Qinghai–Tibet Plateau, The Cryosphere, 16, 4823–4846, https://doi.org/10.5194/tc-16-4823-2022, 2022.

Zhao, L., Ding, Y., Liu, G., Wang, S., and Jin, H.: Estimates of the reserves of ground ice in permafrost regions on the Tibetan plateau, J. Glaciol. Geocryol., 32:1-9, 2010a.

Zhao, L., Wu, Q., Marchenko, S., and Sharkhuu, N.: Thermal state of permafrost and active layer in Central Asia during the international polar year, Permafrost and Periglac. Process., 21, 198–207, https://doi.org/10.1002/ppp.688, 2010b.

Zhao, L. and Sheng, Y.: Permafrost survey manual, Science Press., Beijing, 13–14, 2015.

Zhao, L., Wu, T., Xie, C., Li, R., Wu, X., Yao, J., Yue, G., and Xiao, Y.: Support geoscience research, environmental management, and engineering construction with investigation and monitoring on permafrost in the Qinghai-Tibet plateau, China (in Chinese with English abstract). Bull. Chin. Acad. Sci.;32(10):1159-1168, 10.16418/j.issn.1000-3045.2017.10.015, 2017.

Zhao, L., Hu, G., Zou, D., Wu, X., Ma, L., Sun, Z., Yuan, L., Zhou, H., and Liu, S.: Permafrost Changes and Its Effects on Hydrological Processes on Qinghai-Tibet Plateau, Bull. Chin. Acad. Sci., 34, 1233–1246, DOI: 10.16418/j.issn.1000-3045.2019.11.006, 2019a.

Zhao L, Sheng Y. Permafrost and environment changes on the Qinghai-Tibetan Plateau. Beijing, China: Science Press.; 2019b.

Zhao, L., Zou, D., Hu, G., Wu, T., Du, E., Liu, G., Xiao, Y., Li, R., Pang, Q., Qiao, Y., Wu, X., Sun, Z., Xing, Z., Sheng, Y., Zhao, Y., Shi, J., Xie, C., Wang, L., Wang, C., and Cheng, G.: A synthesis dataset of permafrost thermal state for the Qinghai–Tibet (Xizang) Plateau, China, Earth Syst. Sci. Data, 13, 4207–4218, https://doi.org/10.5194/essd-13-4207-2021, 2021.

Zhao, L., Hu, G., Liu, G., Zou, D., Wang, Y., Xiao, Y., Du, E., Wang, C., Xing, Z., Sun, Z., Zhao, Y., Liu, S., Zhang, Y., Wang, L., Zhou, H., and Zhao, J.: Investigation, Monitoring, and Simulation of Permafrost on the Qinghai-Tibet Plateau: A Review, Permafrost Periglac. Process., 35:412–422, https://doi.org/10.1002/ppp.2227, 2024.

Zhou, C., Cheng, W., Zhao, S., Gao, X., and Nan, W.: Geo-morphological map of Western China (1:1000000). Beijing: Institute of Geographic Sciences and Natural Resources Research, Chinese Academy of Sciences, 2007.

Zou, D., Pang, Q., Zhao, L., Wang, L., Hu, G., Du, E., Liu, G., Liu, S., and Liu, Y.: Estimation of Permafrost Ground Ice to 10 m Depth on the Qinghai-Tibet Plateau, Permafrost Periglac. Process., https://doi.org/10.1002/ppp.2226, 2024.

Zou, D., Zhao, L., Sheng, Y., Chen, J., Hu, G., Wu, T., Wu, J., Xie, C., Wu, X., Pang, Q., Wang, W., Du, E., Li, W., Liu, G., Li, J., Qin, Y., Qiao, Y., Wang, Z., Shi, J., and Cheng, G.: A new map of permafrost distribution on the Tibetan Plateau, The Cryosphere, 11, 2527–2542, https://doi.org/10.5194/tc-11-2527-2017, 2017.

Zou, D., Zhao, L., Wu, T., Wu, X., Pang, Q., and Wang, Z.: Modeling ground surface temperature by means of remote sensing data in high-altitude areas: test in the central Tibetan Plateau with application of moderate-resolution imaging spectroradiometer Terra/Aqua land surface temperature and ground based infrared radiometer, J. Appl. Remote Sens., 8, 083516, https://doi.org/10.1117/1.JRS.8.083516, 2014.